Spring 2024

# Open-ended hollow coaxial cable resonance sensing via permittivity fluctuations for applications to exhaled breath health monitoring

Peter Henry Holtmann
*Missouri University of Science and Technology*

## Recommended Citation

Holtmann, Peter Henry, "Open-ended hollow coaxial cable resonance sensing via permittivity fluctuations for applications to exhaled breath health monitoring" (2024). *Masters Theses*. 8185.
https://scholarsmine.mst.edu/masters_theses/8185

# OPEN-ENDED HOLLOW COAXIAL CABLE RESONANCE SENSING VIA PERMITTIVITY FLUCTUATIONS FOR APPLICATIONS TO EXHALED BREATH HEALTH MONITORING

by

PETER HENRY HOLTMANN

A THESIS

Presented to the Graduate Faculty of the

MISSOURI UNIVERSITY OF SCIENCE AND TECHNOLOGY

In Partial Fulfillment of the Requirements for the Degree

MASTER OF SCIENCE

in

ELECTRICAL ENGINEERING

2023

Approved by:

Jie Huang, Advisor
Kristen Donnell
Charles R. Jones
Steve Watkins

# PUBLICATION THESIS OPTION

This thesis consists of the following article, formatted in the style used by the Missouri University of Science and Technology:

Paper I, found on pages 12-51 has been submitted to *iScience*.

# ABSTRACT

We report a pre-diagnostics breath analyzer based on the open-ended hollow coaxial cable resonator (OE-HCCR) to achieve real-time differentiation of healthy and compromised lung function through electromagnetic analysis of exhaled breath matter. A two-phase amplification scheme of electromagnetic signatures metered via the S11 phase curve offers high sensitivity to permittivity fluctuations in exposed airflow. The mathematical model of the breath analyzer is explained, followed by experimental validation of numerical findings from previous work. The collection of breath transient signals is performed through monitoring the reflected power magnitude and phase of the scattering parameter (S11) at the resonance frequency. Material fluctuations inside the active cavity of the resonator result in changes of the fringing electric field at the open end, which is metered through a shift in resonance frequency. Significant sensitivity amplification occurs near the resonance frequency due to the slope of the S11 phase curve.

Findings indicated that time transient signals corresponding to healthy breaths returned to 10% of their maximum amplitudes within 1 second at the terminus of the breath transient. The time transient signal for exhaled breaths can be subdivided into three distinguishable regions, allowing for further insight into breath matter content. Analyzing each region independently of one another offers insight into the rates of ingress, digestion, and egress of volatile and nonvolatile materials inside the active cavity of the probe throughout different stages of aerosol uptake, residency, and elimination. When the breath transient data is viewed as an integrated and self-consistent composite, additional details on the content of the exhaled breath can be deduced.

# ACKNOWLEDGEMENTS

I would like to take the opportunity to express my gratitude to all the people who helped me along my academic journey towards an M.S. in Electrical Engineering. I’d first like to express my utmost thanks to Dr. Jie Huang for his continuous guidance and generous support over the previous one-and-a-half years. Dr. Huang’s courses laid the firm foundation of knowledge for every aspect of this project and my future work. His constant pursuit of knowledge and discovery will continue to inspire me well beyond my time here at Missouri S&T.

I would like to thank Dr. Jie Huang, Dr. Kristen M. Donnell, and Dr. Steve E. Watkins for serving on my committee.

I am also sincerely grateful to Dr. Rex E. Gerald II for his consistent mentorship during my degree. His eagerness and persistence fueled much of my progress. I hope to one day serve as a mentor who inspires critical thinking, persistence, and personal growth in much the same manner as Dr. Gerald has for me.

I would also like to thank all my colleagues in the Lightwave Technology Lab for their constant support and various lessons throughout our shared time.

Lastly, I would like to thank my parents, siblings, friends, partner, and my dog for their love and support. Despite being clueless (and generally disinterested) towards my projects, their emotional support was crucial to the completion of this project.

# TABLE OF CONTENTS

SECTION

# LIST OF ILLUSTRATIONS

SECTION Page

PAPER

SECTION

# LIST OF TABLES

PAPER Page

# NOMENCLATURE

| Symbol | Description |
|---|---|
| OE-HCCR | Open-Ended Hollow Coaxial Cable Resonator |
| EM | Electromagnetic |
| MOF | Metal-Organic Framework |
| VOC | Volatile Organic Compound |

# 1. INTRODUCTION

The open-ended hollow coaxial cable resonator (OE-HCCR) is a novel sensing technology that demonstrates ultra-sensitivity to variations in gap distance and dielectric properties of the material inside the active cavity of the probe. Previous studies have applied the OE-HCCR to fluctuations of gap distance in a variety of manners (i.e., nanometer displacements [1], hydraulic pressure sensing [2], high-temperature pressure sensing [2], impact sensing [3], and applications as an accelerometer [3]), however, the sensitive nature of the probe to material and/or concentration fluctuations has yet to be explored in greater detail.

Coincidentally, early explorations into permittivity sensing through use of an OE-HCCR aligned with the start of the COVID-19 pandemic. As such, the increased focus on inexpensive, robust, and widely-deployable diagnostic devices for pulmonary diseases set the stage for the development of ultra-sensitive devices for breath analysis. While the OE-HCCR's ability to measure fluctuations in gap distance has allowed for numerous applications in the measurement of pressure, tilt, and other displacement measurements, very little research has focused on chemistry-based sensing applications of the OE-HCCR. Toward this end, the objectives of this thesis are to:

1) Expand the current numerical understanding of the OE-HCCR through a discussion of the phase coupling conditions and their relationship to time-transient signals.

2) Discuss the chemical-sensing ability of the OE-HCCR through the analysis of relative permittivity fluctuations inside the active cavity of the probe.

3) Demonstrate an OE-HCCR breath analyzer for the rapid and binary determination of healthy or compromised lung functions.

4) Propose and demonstrate a new microphonics technique using the OE-HCCR with a thin metal diaphragm, allowing for the assessment of both pressure waves (sound) and material fluctuations (chemical concentrations in air).

The investigation results are presented in a combination of two thesis sections and one submitted journal paper in this thesis and their contents are briefly described as follows.

First, the current understanding of the mathematical basis for the OE-HCCR will be described, focusing on the effect of the relative permittivity inside the device. A phenomenological approach will be taken develop a better understanding of the phase coupling conditions of the resonator.

Next, in Paper I, a breath analyzer based upon the OE-HCCR sensing platform is proposed and validated. Experimental findings focusing on the nature of nonvolatile particles in the active cavity of the resonator will be discussed. Time-transient signals corresponding to exhaled breath will be introduced and analyzed.

Following Paper I, an institutional review board-approved study for the collection of exhaled breath time-transient signals will be introduced. The results of the study as of November 29th, 2022 will be discussed. Further, common features across all collected breath transients will be interpreted for a detailed analysis of the breath profiles.

Lastly, a modified OE-HCCR sensing platform will be proposed for the simultaneous collection of sound and permittivity information. Experimental findings will be validated using separate sensors for the singular detection of sound waves and permittivity fluctuations. Recommendations for future work are offered for the continued development of this sensing technique.

# 2. BACKGROUND

Figure 2.1 shows a schematic diagram of the OE-HCCR. The diameters of the inner and outer conductors are denoted as *2a* and *2b*, respectively. While traditional coaxial cables would have a dielectric layer between the two conductors, here the dielectric is removed and replaced with air. A metal plate is affixed at the open end of the hollow coaxial cable. The thickness of the air dielectric in the gap between the open end and the metal plate is *d*. A grounded flange with an infinite diameter is assumed for the model. A metal post is welded within the hollow coaxial cable, shorting the inner conductor to the outer conductor, resulting in a rise in the storage of magnetic energy in proximity to the post. This storage of magnetic energy creates a large impedance mismatch, leading to a high reflection point to the electromagnetic (EM) wave propagating through the coaxial cable [1].

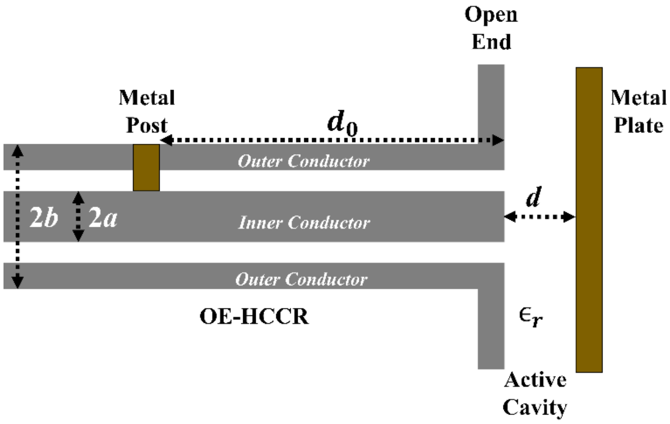

Figure 2.1: Schematic diagram of an OE-HCCR terminated by a metal plate-backed air dielectric layer with a gap thickness of *d*. The metal post serves as the first reflector, and the open end serves as the second reflector. $\epsilon_r$ is the relative permittivity of the active cavity.

To view the OE-HCCR through the perspective of an equivalent circuit, the metal post is represented by a shunt inductor *L* and a series shunt resistor *R*. Thus, the reflection coefficient ($r_1$) caused by the metal post can be expressed as (1) and (2):

$$r_1 = \Gamma_1 e^{j\phi_1} = \frac{R+j\omega L-Z_0}{R+j\omega L+Z_0} \tag{1}$$

$$\phi_1 = \pi - tan^{-1}\left(\frac{\omega L}{Z_0-R}\right) - tan^{-1}\left(\frac{\omega L}{Z_0+R}\right) \tag{2}$$

where $\Gamma_1$ and $\phi_1$ represent the magnitude and phase of the reflection coefficient, respectively; $Z_0$ is the characteristic impedance of the hollow coaxial cable; and $\omega$ is the angular frequency of the input signal. In the high-frequency region (e.g., $f$ > 3 GHz), acapacitor ($\Delta C$) should also be considered in the equivalent circuit model.

The open end of the hollow coaxial cable can simply be considered an open circuit, causing approximately 100% reflection of the EM wave. An open circuit can be modeled simply as a shunt capacitance *C* in the equivalent circuit. Thus, the reflection coefficient ($r_2$) for the open end can be expressed as (3) and (4):

$$r_2 = \Gamma_2 e^{j\phi_2} = \frac{1-j\omega Z_0 C}{1+j\omega Z_0 C} \tag{3}$$

$$\phi_2 = -2\, tan^{-1}(\omega Z_0 C) \tag{4}$$

where $\Gamma_2$ and $\phi_2$ represent the magnitude and phase of the reflection coefficient, respectively. The shunt capacitance due to the disturbed fringing field at the open end, employing the spectral domain analysis, is given by (5):

$$C = \epsilon_r (C_1 + C_2) \tag{5}$$

$$C_1 = \frac{2\epsilon_0}{[ln(b/a)]^2} \int_a^b \int_a^b \int_0^\pi \frac{cos\,\phi' d\rho d\rho' d\phi'}{\sqrt{\rho^2+\rho'^2-2\rho\rho'\,cos\,\phi'}} \tag{6}$$

$$C_2 = \frac{4\epsilon_0}{[\ln(b/a)]^2} \sum_{\mathrm{n}=1}^{\infty} \int_a^b \int_a^b \int_0^\pi \frac{\cos\phi' d\rho d\rho' d\phi'}{\sqrt{\rho^2+\rho'^2+4n^2d^2-2\rho\rho'\cos\phi'}} \tag{7}$$

where $\rho$ and $\rho'$ denote the radial direction and $\phi'$ denotes the azimuthal direction. Note that $C_1$ is essentially the static capacitance at the open end when the gap distance $d$ is infinite; $C_2$ is an additional variable to compensate for the finite thickness of the air dielectric [4].

Assuming a microwave signal with a frequency *f* is launched into the OE-HCCR, the signal will encounter a series of reflectors. First, the input signal will be partially reflected by the metal post. The transmitted portion of the signal will then resonate in the coaxial structure, being reflected back and forth between the metal post and the open end. With each reflection at the metal post, a portion of the signal is coupled out of the OE-HCCR. Summing the waves coupled out at the first reflector yields the reflection coefficient (*r*) of the OE-HCCR:

$$r = \frac{r_1^* - r_2 e^{-\alpha 2 d_0 - j\delta}}{1 - r_1 r_2 e^{-\alpha 2 d_0 - j\delta}} = \frac{\Gamma_1 e^{-j\phi_1} - \Gamma_2 e^{j\phi_2} e^{-\alpha 2 d_0 - j\delta}}{1 - \Gamma_1 e^{-j\phi_1} \Gamma_2 e^{j\phi_2} e^{-\alpha 2 d_0 - j\delta}} \tag{8}$$

where $d_0$ is the distance between the first and second reflectors; $\alpha$ is the transmission loss of the hollow coaxial cable; $\delta = \frac{4\pi d_0 f}{c}$ denotes the round-trip phase delay between two partially reflected waves; and $c$ is the speed of light in vacuum. The superscript asterisk "*" denotes the complex conjugate. The magnitude (*M*) of the reflection coefficient can then be obtained:

$$M = \sqrt{\frac{\Gamma_2 - 2\Gamma_1 \Gamma_2 e^{-\alpha 2 d_0} cos(\delta - \phi_1 - \phi_2) + \Gamma_2^2 e^{-\alpha 4 d_0}}{1 - 2\Gamma_1 \Gamma_2 e^{-\alpha 2 d_0} cos(\delta - \phi_1 - \phi_2) + \Gamma_1^2 \Gamma_2^2 e^{-\alpha 4 d_0}}} \tag{9}$$

Further, solving (9), we have

$$M = \sqrt{1 + \frac{\left(\Gamma_1 - \Gamma_2 e^{-\alpha 2 d_0}\right)^2 - \left(1 - \Gamma_1 \Gamma_2 e^{-\alpha 2 d_0}\right)^2}{\left(1 - \Gamma_1 \Gamma_2 e^{-\alpha 2 d_0}\right)^2 + 4\Gamma_1 \Gamma_2 e^{-\alpha 2 d_0} sin^2 \frac{\delta - \phi_1 - \Phi_2}{2}}} \tag{10}$$

Since $0 < \Gamma < 1$, the magnitude of the reflection coefficient of the OE-HCCR is minimized when the phase term in (10) satisfies the condition in (11):

$$sin^2 \frac{\delta-\phi_1-\phi_2}{2} = 0 \rightarrow \delta - \phi_1 - \phi_2 = 2m\pi, m = 0,1,2,3 \ldots \tag{11}$$

The “analytical” expression for the resonance frequencies (i.e., when the magnitudes reach a series of local minimum values), can be obtained by substituting $\delta = \frac{4\pi d_0 f}{c}$ into (11):

$$\frac{4\pi d_0 f_{res}}{c} - \phi_1 - \phi_2 = 2m\pi \rightarrow f_{res} = \frac{c(2m\pi+\phi_1+\phi_2)}{4\pi d_0} \tag{12}$$

(12) clearly reveals that the fundamental resonance frequency of the OE-HCCR is a function of $\phi_1$ and $\phi_2$ (i.e., the phases of the reflection coefficients of the two reflectors). Thus, the sensing capability of the OE-HCCR is predicated on changes to $\phi_2$, since $\phi_1$ will is held constant. Specifically, according to equation (3), the phase of $r_2$ is a function of the fringing capacitance at the open end, which depends exponentially upon the gap distance between the metal plate and the open end of the coaxial cable. Recall from (4) that changes in $\phi_2$ are the result of changes in capacitance, since $\omega$ and $Z_0$ are unchanging. Further, changes in capacitance are due to variations in either the gap distance (*d*) or the relative permittivity inside the active cavity ($\epsilon_r$). Consequently, when either of these two parameters varies slightly, changes in the fringing capacitance lead to changes in both the magnitude and phase of $r_2$. The change in $\phi_2$ results in a shift of the resonance frequency. By tracking the frequency shift of the reflection spectrum, the movement of the metal plate can be accurately determined, assuming the material inside the active cavity of the probe is held constant. Alternatively, the relative permittivity inside the active cavity can be determined given that the gap distance is unchanged. Thus, any physical parameter that can

be correlated to the movement of the metal plate (e.g., displacement, or deflection under pressure) or any replacement of material inside the active cavity can be accurately measured by the proposed OE-HCCR by tracking the resonance frequency shift, assuming changes are only occurring to one parameter at a time. However, since $\phi_1$ and $\phi_2$ are functions of frequency, (12) has no analytical solution [4].

# 3. OE-HCCR PHASE COUPLING

The coupling coefficient of resonators is a concept used often in discussions regarding microwave filters. In the case of the OE-HCCR, the most important distinction is that of critical coupling. Critical coupling occurs through the modification of either gap distance or effective permittivity inside the active cavity and is defined as the condition where the modification of these parameters results in the largest resonance of the reflected wave [5]. Combinations of the two parameters that result in a resonance at lower frequencies than that of critical coupling are considered loosely-coupled, whereas those resulting in a resonance at higher frequencies than that of critical coupling are considered over-coupled. Our analysis of the coupling coefficient, however, focuses rather on the phase of the reflected wave near the resonance frequency. This is due to the large rate of change of the phase near resonance, allowing for an amplification of dielectric sensitivity. To distinguish between discussions of coupling in regards to the magnitude power loss versus the phase of the reflected wave, we will be denoting the different phase coupling conditions as one word rather than the hyphenated notation seen previously: *overcoupled* and *undercoupled*. Importantly, no experiments were conducted when the resonator was critically coupled. This state occurs at a singular, unstable point along the frequency axis, meaning that any modification of either the gap distance or effective permittivity inside the active cavity would dislodge the probe from this condition. With that said, it is possible for the resonator to shift from one condition to another, having passed through a state of critical coupling for an instant. Trials in which this occurred were typically dismissed, as interpretation of a breath transient requires significant post-processing to account for the change in conditions.

## 3.1. UNDERCOUPLING

Undercoupling of the probe occurs when the resonance frequency is greater than the frequency at which critical coupling would occur. Early experiments referenced throughout this thesis were performed when the probe was in an undercoupled state. Breath transients are collected by monitoring the phase curve at a single frequency while breath enters and then subsequently evaporates in the probe. Figure 3.1 shows the typical behavior of an undercoupled phase response as well as the resulting breath transient signal.

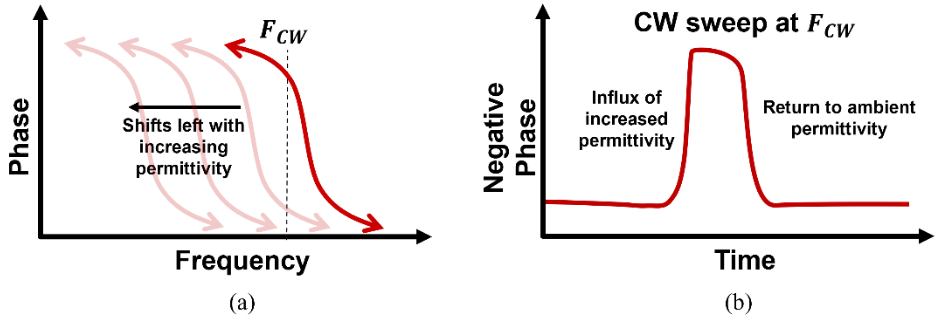

(a) (b)

Figure 3.1: (a) The typical nature of an undercoupled phase response during an influx of material with higher permittivity than the ambient air originally inside the active cavity of the resonator. (b) The breath transient response corresponding to an undercoupled phase condition. Notice the breath transient has been negated for simplified analysis.

## 3.2. OVERCOUPLING

Overcoupling of the probe occurs when the resonance frequency is greater than the frequency at which critical coupling would occur. For the purposes of this thesis, most experiments were performed with the resonator probe in the overcoupled state. Figure 3.2

demonstrates the typical behavior of an overcoupled resonator along with the corresponding breath transient signal.

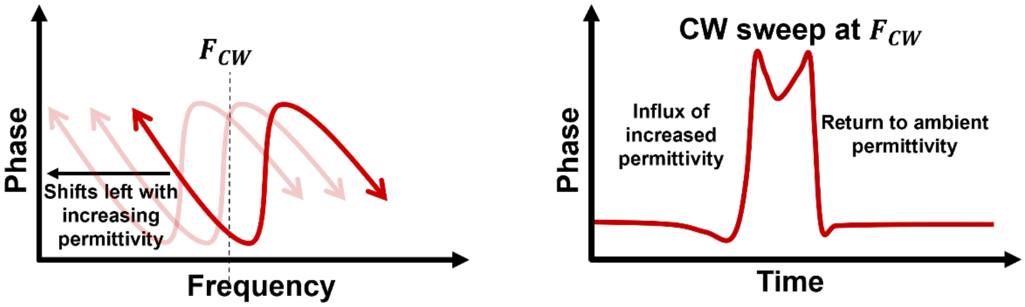

(a) (b)

Figure 3.2: (a) The typical nature of an overcoupled phase response during an influx of material with higher permittivity than the ambient air originally inside the active cavity of the resonator. (b) The breath transient response corresponding to an overcoupled phase condition. Notice the two peak features, which result from the change in polarity of the phase curve at the CW frequency.

# PAPER

## I. A NOVEL BREATH ANALYZER PROBE FOR THE REAL-TIME SURVEY OF HEALTHY AND COMPROMISED LUNG FUNCTION THROUGH BREATH MATTER CONTENT

### ABSTRACT

Advances in the analysis of exhaled breath condensate for the detection and diagnosis of diseases have allowed for the adoption of rapid, noninvasive tests of pulmonary function. However, existing technologies for exhaled breath analysis rely on expensive, obscure, and nondeployable collection methodologies. In this article, we report a pre-diagnostics breath analyzer based on an open-ended hollow coaxial cable resonator (OE-HCCR) to achieve real-time differentiation of healthy and compromised lung function through electromagnetic analysis of exhaled breath matter. The OE-HCCR breath analyzer offers high sensitivity to abnormalities in exhaled breath with no additional enhancements due to its two-phase amplification scheme of electromagnetic signatures from exposed airflow. The mathematical model of the breath analyzer is detailed, followed by experimental validation of numerical findings. Our analysis is based upon acquired breath transients typically 7 +/- 3 seconds in length. Further, findings indicate that a healthy breath transient will return to 10% of their maximum amplitude within 1 second of the signal's second peak whereas elongation of the signal's tail is characteristic of high quantities of respiratory droplets in breath and, thus, of compromised lung function. The novel OE-

HCCR breath analyzer offers an inexpensive, robust device for the binary detection of compromised pulmonary function and is capable of large-scale deployment in hospitals, minute clinics, and common commercial environments.

# 1. BACKGROUND

Tests of pulmonary function fulfil a crucial role in medical practice. Diagnoses such as the obstruction of airways, identification of risk factors for several diseases, and assessment of prognosis and severity can often be determined through a variety of pulmonary function tests. In recent years, tests have increased in complexity and selectivity, limiting the applications of each test to a handful of useful diagnoses. Tests of pulmonary function range from traditional techniques such as measures of exhaled breath flow [1]–[3] and the analysis of lung tissue [4], [5] to cutting edge techniques that examine breath content for the detection of select diseases.

Traditional tests of pulmonary function overlook valuable information regarding an individual’s overall health due to their failure to inspect breath matter content. Technological advances in the measurement, quantification, and identification of particulates in exhaled breath have opened exciting opportunities for rapid, non-invasive detection of diseased or compromised lungs. Further, due to the narrow specificity of each traditional test of pulmonary function, diseases of the lungs or impaired lung functionality are often not detected at the onset of symptoms. Several studies suggest that over half of all cases of COPD go undiagnosed [6], [7] leading to increased rates of lung cancer and other serious ailments [7].

## 1.1. TRADITIONAL TESTS OF PULMONARY FUNCTION

The most common practices for the quantification of lung function are through techniques such as the use of stethoscopes [8], spirometry [9], impulse oscillatory [10], plethysmography [11], X-ray imaging [12], pulse oximetry [13], and lung biopsy [13].

Spirometry is a simple, noninvasive test of pulmonary function that measures the volume of air expired and inspired from an individual’s lungs as a function of time. Through spirometry, volume and flow of breath are measured against time. These measurements are expressed by several values that can be used in the detection and diagnosis of lung disease. The values include: the forced expiratory volume (FEV1); the maximum volume of air exhaled when blowing as fast as possibly, called forced vital capacity (FCV); peak expiratory flow (PEF), the maximum flow that is exhaled when breathing at a steady rate; and inspiratory vital capacity (IVC), the maximum volume of air that an individual can inhale after fully depleting their lungs [3]. Spirometry has been used for the assessment and prediction of a variety of lung diseases, including chronic obstructive pulmonary disease (COPD), asthma [14], and lung cancer [15]. However, spirometry results by no means yield a definitive diagnosis. While the technique has high diagnostic accuracy for COPD, asthma must generally be confirmed through other techniques (e.g., nitric oxide measurements) [16]. The same is true for lung cancer, where a spirogram is one of several tests that is necessary to support the diagnosis of disease [15]. Several assessments of pulmonary function similar to spirometry have become popular in recent years, such as impulse oscillometry [10] and plethysmography [11], but these techniques generally have the same limitations of detection as encountered in spirometry.

X-ray computed tomography (X-ray CT) offers another means of detecting diseased lungs or depleted pulmonary function through its use of noninvasive imaging [17]. High resolution computed tomography (HRCT) is widely considered the “gold-standard” for the detection or monitoring of several pulmonary diseases, most notably cystic fibrosis. However, the consistent use of CT can lead to significant radiation doses in patients, creating the need for ionizing radiation-free CT methods that are still in their infancy [17].

Pulse oximetry uses two light emitting diodes and a photodetector to determine the concentration of oxygen in an individual’s blood and is a simpler means of indirectly testing pulmonary function. A quantity of the transmitted LED light will be absorbed by the tissue between the light source and the photodetector (typically a finger or ear), which then allows a microprocessor to calculate the concentrations of oxyhemoglobin and deoxyhemoglobin using the difference between the light emitted and received. These two values are then used to calculate the hemoglobin oxygen saturation in arterial blood [18]. While decreased pulse oximetry values have been associated with reduced pulmonary function, the technique’s applications towards diagnostics are limited [13].

Lastly, a much more invasive test of pulmonary function is that of lung biopsy. During a biopsy a select area of tissue is removed for examination under a microscope. Open lung biopsy occurs when a patient is under general anesthesia and a surgeon creates an incision to surgically remove a section of lung tissue. In closed lung biopsies, the surgeon will collect lung tissues typically using a needle, either by penetration of the skin or through the trachea [4]. Biopsy has served as an effective tool for acute respiratory distress syndrome (ARDS), with several studies attributing the technique to having a significant impact on a patient’s survivability outcomes. However, the technique is much more invasive than other tests of pulmonary function, resulting in higher overall complication rates [4].

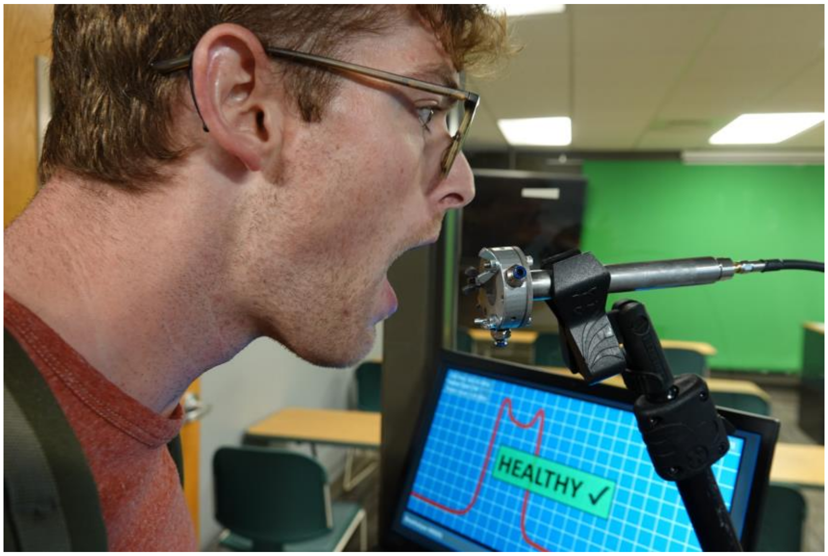

Figure 1: The proposed setting of a deployed OE-HCCR Breath Analyzer.The robust and inexpensive nature of the OE-HCCR breath analyzer allows for large-scale deployment pre-diagnostic screening devices in high-traffic areas, as opposed to traditional tests of pulmonary function which are limited to use in clinical environments. Installation of the breath analyzer systems at homes, grocery stores, pharmacies, and medical clinics will significantly increase daily accessibility to on-demand accurate testing and thereby mitigate the spread of infectious pathogens and prevent pulmonary diseases going undiagnosed.

One measurement that these traditional tests of pulmonary function fail to collect is that of breath matter. Recent advances in technologies aimed at measuring, quantifying, and identifying particulates in exhaled breath has opened exciting opportunities for rapid, non-invasive detection of diseased or compromised lungs. Further, due to the narrow specificity of each of the traditional tests of pulmonary function, diseases of the lung or impaired lung functionality are often not detected at the onset of symptoms. Several studies suggest that over half of all cases of COPD go undiagnosed [6], [7] leading to higher rates of lung cancer and other serious diseases of the lung [7]. Lastly, these diagnostic tools are often limited in use due to the clinical environments required for their deployment. An inexpensive and robust diagnostic tool that is deployable to nonclinical environments is necessary to prevent the spread of pulmonary infections while the infection is still in the prodromal stage.

Table 1: Complementary diagnostic methods assessing compromised lung function. *With additional methods for specificity.

| Measurand | Methods | | | | |
|---|---|---|---|---|---|
| | Spirometry | X-Ray CT | Oximetry | Biopsy | **OE-HCCR Breath Analyses** |
| Lung Capacity Parameters<br>(FEV$_1$, FCV, PEF, IVC) | ✓ | X | X | X | ✓ |
| Cancer Stage Analysis | X | ✓ | X | ✓ | ✓ |
| Blood Oxygen<br>Oxygenated vs. Deoxygenated Hemoglobin | X | X | ✓ | X | X |
| Other Considerations | | | | | |
| Approx. Instrument Cost < $5000 | ✓ | ✓ | ✓ | X | ✓ |
| Approx. Cost Per Test < $10 | X | X | X | X | ✓ |
| Low Maintenance Cost | X | X | ✓ | N/A | ✓ |
| Diagnostic Time < 30 min | ✓ | X | ✓ | X | ✓ |
| Service Life > 5 Years | ✓ | ✓ | ✓ | N/A | ✓ |
| Portability | X | X | X | X | ✓ |
| Non-invasive Test | ✓ | X | ✓ | X | ✓ |

## 1.2. BACKGROUND AND ADVANTAGES OF RESPIRATORY DROPLET AND PARTICULATE ANALYSES FOR DETECTION OF COMPROMISED PULMONARY FUNCTION

Exhaled breath condensate (EBC) can be separated into two distinct categories: volatile and nonvolatile materials. Exhaled breath volatiles are largely comprised of inorganic compounds such as ammonia, nitrogen, oxygen, water, carbon dioxide, and trace amounts of volatile organic compounds (VOCs) [19]. Exhaled breath nonvolatiles, on the other hand, include pathogen-laden respiratory droplets. Highly transmissible diseases, including SARS-CoV-2, are primarily transmitted via droplets or aerosols (i.e., respiratory droplets that contain virions capable of replication and infection in susceptible individuals) [20]. As a result, the assessment of an individual's level of contagion (i.e., the likelihood that an individual can infect others around them) via pharyngeal swabs or other deterministic survey of disease may not be accurate during early stages of the infection. Exhaled breath, thus, may serve as a more suitable sample for the evaluation of an individual's level of infection in the prodromal stage. Respiratory infectious pathogens are generally reported to spread through three transmission routes — namely contact transmission, droplet transmission, and aerosol transmission [21], [22] — and are generated through a variety of mechanisms. Literature supports five main generation mechanisms of RDs [21]: (1) the closing and reopening of the mouth [23], (2) closing and reopening of vocal ford [24], (3) closing and reopening of small airways [25], (4) reopening and closing of the pores of Kohn [26], and (5) the rupture of liquid films that line the respiratory tract (RT) [27]. The size distribution of these droplets varies largely with their point of origin (which is directly related to the respiratory activity performed; i.e., breathing, coughing, talking, etc.) [28], but reports in pulmonary literature suggest that the size of droplets capable of pathogen transmission are those with diameter less than one micron [29]. Current methods for the collection and analysis of these RDs typically rely on complex apparatuses that employ solid impaction, liquid impaction, or high-speed photography to quantify the particles and characterize the size distribution of the droplet swarms [21]. However, due to the time-extensive nature of these analyses, their application for real-time survey of human populations is quite limited. Further, literature suggests that a standardize means of particle collection is necessary to determine the efficacy of these different techniques [21].

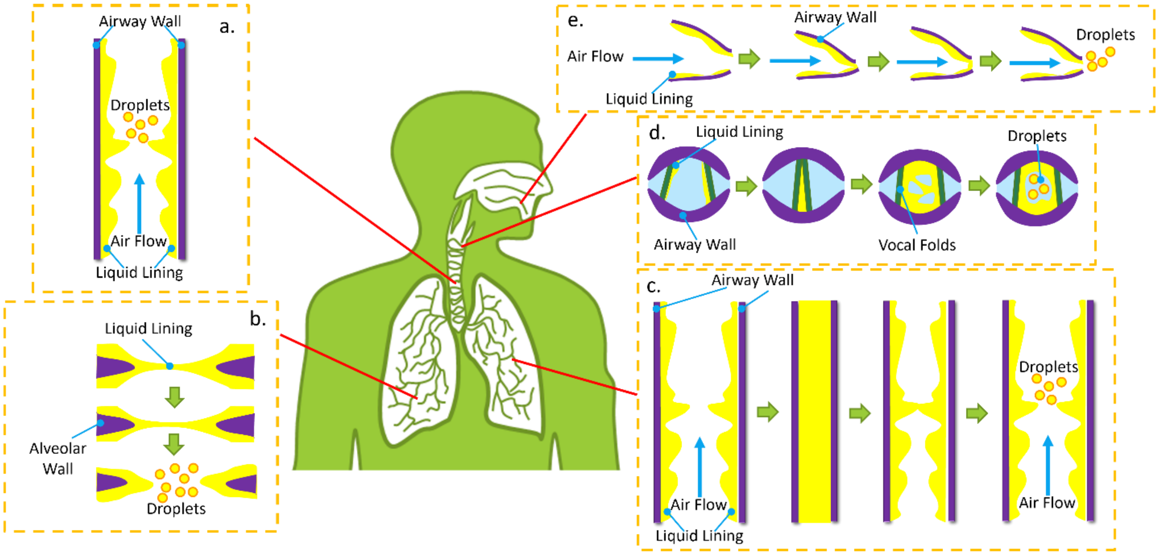

Figure 2: Generation mechanisms of respiratory droplets (RDs) at five key sites: (a) rupture of liquid film lining the respiratory tract (RT), (b) closing and reopening of the pores of Kohn, (c) closing and reopening of small airways, (d) closing and reopening of vocal folds, and (e) closing and reopening of the mouth [21].

In this work, a novel breath analyzer technology provides a simple, robust binary output survey tool for the preliminary detection of healthy and unhealthy pulmonary function in real-time. The tool may prove effective for early detection of disease states via the analysis of breath composition, namely respiratory droplet concentration. It may also help with monitoring recovery therapies. The technology utilizes microwave resonance to detect changes in permittivity of the exhaled breath, resulting in sufficient sensitivity to detect the presence of pulmonary diseases or depleted pulmonary function as well as to discern lung function states. The breath analyzer does not yet aim to distinguish between specific diseases or serve as a narrowly focused diagnostics tool. Rather, it focuses on determining if further testing is required of an individual to identify which pulmonary disease is likely present, allowing for the rapid survey of several individuals using a device that is more robust, inexpensive, and recyclable than other tests of pulmonary function.

The novel technique was experimentally verified using a lab-built open-ended hollow coaxial cable resonator (OE-HCCR). The achieved sensitivity is due to two signal amplification processes that allow for ultrasensitive detection of poor lung function collected in a noninvasive manner. First, a mathematical model for the breath analyzer will be discussed to understand the fundamental physics of the technology. Second, through experimentation, we compare the proposed breath analyzer to classical methods for determining lung function (i.e., spirometry), propose a breath pattern to maximize droplet production, and showcase preliminary results collected from several individuals using this breath analyzer. Supportive evidence shows that numerical investigations of this technology match well with experimental results, affording more sensitivity to depleted lung function while maintaining the participants' level of comfort during the data collection process. Table 1 highlights the complimentary nature of the proposed breath analyzer when compared to the previously discussed diagnostic methods for the detection of compromised lung function.

# 2. PROBING THE THEORETICAL ULTIMATE LIMIT OF THE PROPOSED OE-HCCR BREATH ANALYZER

In early 2021, a prototype benchtop OE-HCCR breath analyzer was fabricated and tested to verify its ultrahigh sensitivity and low limit of detection. The key feature of the proposed OE-HCCR breath analyzer is the two-stage amplification scheme, which allows for resolutions that exceed nanometer scale common to advanced laser interferometer systems [30]. The OE-HCCR is formed by two electromagnetic (EM) wave reflectors in a hollow RF coaxial cable. These reflectors take the form of a metal post that connects the inner and outer conductors part way down the length of the OE-HCCR and the open end of the coaxial cable, as illustrated in Figure A2 in supplemental materials.

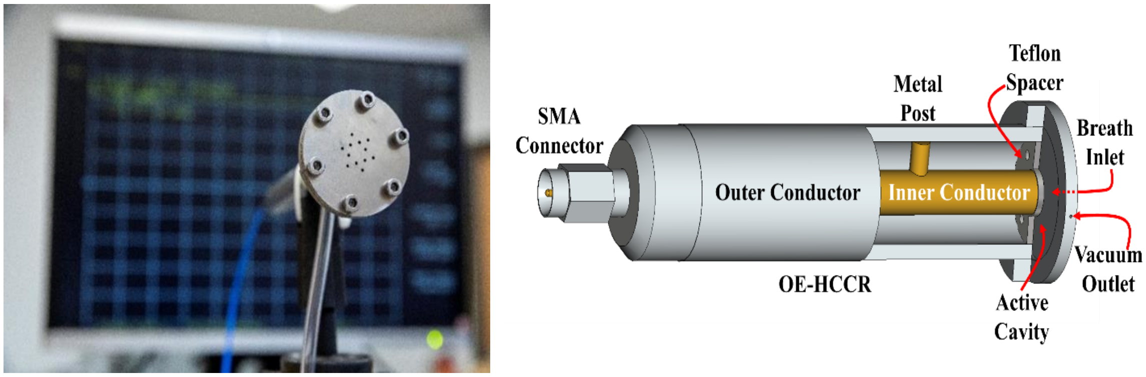

(a) (b)

Figure 3: Real and modeled OE-HCCR Breath Analyzers. (a) Prototype 6mm inner conductor OE-HCCR Breath Analyzer Probe head with attached coaxial cable and vacuum tubing; (b) 3-demensional model of 6mm inner conductor Breath Analyzer Probe with viewing cutaway in outer conductor, showcasing the first reflector (metal post) and active cavity of the probe.

A porous metal plate is fitted to part of the OE-HCCR at a distance d away from the open end of the coaxial cable. The transverse EM wave mode in the OE-HCCR excites a fringing electric field at the end of the coaxial cable. Importantly, as the gap distance d decreases, the fringing electric field at the open end of the coaxial cable increases dramatically. Thus, the smaller the gap distance, the larger the electric field and the higher the sensitivity to the OE-HCCR to changes of dielectric properties within the medium of the active cavity formed between the open end of the coaxial cable and the metal plate.

The OE-HCCR can be mathematically described as an equivalent circuit. In this representation, the open end of the coaxial cable can be modeled simply as an effective capacitance that contains the fringing electric field. Importantly, the effective dielectric property of the active cavity is directly related to the capacitance. Employing spectral domain analysis, the capacitance is given by 1:

$$C = \epsilon_r \{ \frac{2\epsilon_0}{[ln(b/a)]^2} \int_a^b \int_a^b \int_0^\pi \frac{cos\phi' d\rho d\rho' d\phi'}{\sqrt{\rho^2 + \rho'^2 - 2\rho\rho' cos\phi'}}$$

$$+ \frac{4\epsilon_0}{[ln(b/a)]^2} \sum_{n=1}^{\infty} \int_a^b \int_a^b \int_0^\pi \frac{cos\phi' d\rho d\rho' d\phi'}{\sqrt{\rho^2 + \rho'^2 + 4n^2 d_1^2 - 2\rho\rho' cos\phi'}} \} \tag{1}$$

where a and b represent the radial size parameters of the coaxial cable, and $\epsilon_r$ and $\epsilon_0$ are the permittivities of the active cavity and vacuum, respectively. The capacitance sensitivity (i.e., the change in capacitance over change in dielectric constant of the active cavity), $\frac{\Delta C}{\Delta \epsilon_r}$, is a function of the gap distance *d*; the thinner the gap, the higher the capacitance and sensitivity. The phase reflection coefficient of the open end of the coaxial cable ($\phi_2$) and its dependence on the dielectric constant of the active cavity can be expressed as 2:

$$\phi_2 = -2tan^{-1}(2\pi f Z_0 C)$$

$$\Delta\phi_2 = \frac{4\pi f Z_0 1}{1+4\pi^2 f^2 Z_0^2 C^2}\frac{\Delta C}{\Delta\epsilon_r}\cdot\Delta\epsilon_r = M_1\cdot\Delta\epsilon_r \tag{2}$$

where f is the interrogation microwave frequency and $Z_0$ denotes the characteristic impedance of the coaxial cable. $M_1$ denotes the coefficient, termed the first-stage dielectric sensitivity. According to equations A1 and A2 (found in supplemental material), the dielectric property of the gap medium is directly encoded into the phase reflection coefficient of the open end of the coaxial cable. Further details on the two-stage amplification scheme are available in the supplemental materials.

## 3. APPLICATION OF THE OE-HCCR PROBE TO EXHALED HUMAN BREATH ANALYSIS

With the two-stage amplification scheme now detailed, theoretical evidence for the OE-HCCR's application as a breath analyzer is assessed through its ability to correctly analyze breath content. When the gap distance is greater than 0.127 mm, the OE-HCCR is overcoupled, resulting in a negative dielectric sensitivity. The absolute value of the dielectric sensitivity increases exponentially as the gap distance decreases. The sensitivity peaks when the coaxial resonator is tuned to the point of critical coupling, where a phase sensitivity greater than -110 degree phase change per one part-per-million (ppm) change in permittivity occurs over a dynamic range of approximately 1 ppm in permittivity. When tuning to the undercoupled zone (i.e., the gap distance is less than 0.127 mm), the dielectric sensitivity jumps to a positive value and decreases as the gap distance decreases. Note that the second-stage phase-amplification factor dominates in the optimized operation of the OE-HCCR. Therefore, the OE-HCCR should be ideally tuned to operate as close to the critical coupling point as possible to achieve ultra-high dielectric sensitivity and concomitantly an ultra-low limit of detection. It is important to note that the critical coupling point of the OE-HCCR can be tuned by changing the size and shape of the metal shorting post or by changing the gap distance of the probe [30].

By filling the active cavity with exhaled human breath, the change in permittivity of the cavity allows our ultra-high sensitivity breath analyzer to analyze the sample by monitoring the generated phase signal. An inhomogeneous breath filled with breath particulates will cause a unique signal response due to the variation in permittivity when compared to an ordinary homogeneous breath. The increase in the permittivity will increase the capacitance at the open end, thus changing the phase reflection coefficient of the open end of the coaxial cable [31], which is subsequently amplified by the resonance-based phase-shift amplification scheme.

Healthy human breath is composed of volatile gases, primarily water and to a significantly lesser extent carbon dioxide and nitrogen. In addition to these volatile gasses, an unhealthy breath also contains nonvolatile matters that are indicative of compromised lungs. The water component of healthy breath produces the largest response of the probe due to the high permittivity of water, masking the extremely small signals from nonvolatile materials found in unhealthy breath. This masking effect dissipates due to the volatile nature of water, leaving the nonvolatile materials and their measurable additive signals. Importantly, the OE-HCCR resonant circuit and interrogator are not saturated or incapacitated by the large permittivity of water. Thus, the OE-HCCR breath analyzer, without any modifications, measurement dead-times/recover-times, and recalibration requirements can be used to measure the amount of nonvolatile matter remaining in the active cavity from an exhaled breath. An inhomogeneous breath, which contains volatile and nonvolatile materials, will be drawn in and fill the cavity as breath is exhaled. As the volatile materials disperse, the nonvolatile materials unique to compromised lung function will remain, creating a very small change in the relative permittivity inside the probe. Furthermore, changes in the relative permittivity of the active cavity, caused by this influx of matter into the probe's cavity, can be accurately metered by the ultra-high sensitivity microwave resonator. Discussions of the physical parameters of the probe in relation to theoretical expectations are discussed in [30].

## 4. PRELIMINARY EXPERIMENTAL RESULTS OF THE OE-HCCR BREATH ANALYZER PROBE

Preliminary experiments were conducted using two sizes of OE-HCCR probes. The two probes, referenced by the size of their central conductors (i.e., 2mm probe and 6mm probe), have their dimensions listed in table 2. The size variation is primarily to test two similar probes with different target consumers; the 6mm probe being used in commercial settings (i.e., doctors' offices, pharmacies, in-patient care) and the 2mm probe being used in personal use. Long term plans for the 2mm probe aim to implement it in an array of several resonators to detect diseases and as a travel-sized vaporlizer for the personal assessment of diseased state.

To support the validity of the OE-HCCR as a breath analyzer, the results of five experiments will be discussed: (1) we demonstrate the offset of the generated phase signal from its initial value once a nonvolatile material enters the active cavity of the probe and, further, the methods used to mitigate the masking effect generated by volatile materials inside the cavity; (2) we compare two generated phase signals, the first being from a flow of ambient air and the second being an exhaled breath, to demonstrate the phase signal's dependence on variations of material or material abundance inside the active cavity; (3) we expose the probe to comparable flows of ambient air and human breath delivered via diaphragm to further the argument made in demonstration 2; (4) we vary the manner of the researcher's breathing before exhaling into the probe to determine if modulations of breathing style generate greater signal response; and (5) we examine several breath tests from four unique individuals to identify common features and discuss potential explanations for variations in signal response.

Table 2: Operating parameters of the two breath analyzer probes

| | **2mm Probe** | **6mm Probe** |
|---|---|---|
| Inner Conductor OD | 2 mm | 6 mm |
| Outer Conductor ID | 5 mm | 14 mm |
| Outer Conductor OD | 9 mm | 18 mm |
| Post Diameter | 1.5 mm | 3 mm |
| Distance from Open End to Post | 40 mm | 75 mm |
| Total Probe Length | 71.5 mm | 130 mm |
| Operating Frequency Range | 2 GHz to 2.4 GHz | 500 MHz to 550 MHz |

## 4.1. SIMULATION OF PHASE BUILDUP FROM NONVOLATILE MATTERS

To demonstrate the offset in signal generated by a nonvolatile material, we monitored the phase response as a known volume of nonvolatile material entered the active cavity, which was then filled with volatile materials. First, we connected the active cavity of the 2mm probe to a vacuum pump, creating constant pressure. Dipping a known length of cleaved and cleaned 125 micron diameter glass optical fiber into the active cavity generated an obvious offset from the initial phase signal generated by only the constant pressure. Then, with the optical fiber acting as our nonvolatile secured in place, we delivered a volatile cleansing solution, 1,1-Dioflouroethane (DFE), into the active cavity. DFE is commonly used to cleanse our probe of any residual materials not evacuated by the vacuum. This experiment measured unwrapped phase against time, using a constant CW frequency of 4.399 GHz. In later experiments, the CW frequency will be noted as well since slight variations to probe tuning can change the CW frequency.

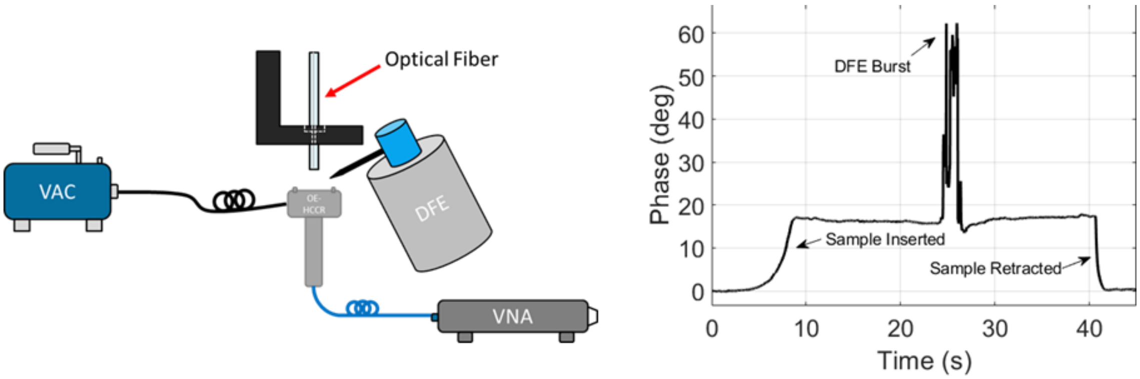

(a) (b)

Figure 4:Simulation of phase signal offset from nonvolatile stimulant. (a) Initial experimental setup for the simulation of the phase signal offset generated by a nonvolatile simulant (optical fiber). Here, the nonvolatile material enters the active cavity, followed by an influx of a volatile material (1,1-Diflouroethane). This is analogous to an exhaled breath containing respiratory droplets, where the volatile gasses in breath are represented by the DFE and the nonvolatile droplets are represented by the fiber. (b) Rise and Fall of the generated signal due to the exposure and subsequent evacuation of a volatile compound (DFE) in addition to the offset phase signal generated by a nonvolatile material (optical fiber).

As seen in Figure 4, a phase offset was generated once the nonvolatile material entered the active cavity. Once the active cavity was filled with our volatile compound, the signal increases significantly only to quickly return to the offset level. Note that, in Figure

5, the initial phase value of each trial is arbitrary and was normalized to zero for ease of interpretation. This will be the standard for all datasets discussed.

To further our analysis, a second experiment was constructed in which a wetted optical fiber was inserted into the active cavity of the probe. In this experiment, the volatile (water droplet) and nonvolatile (optical fiber) materials enter the active cavity at roughly the same time, as they would in the case of exhaled breath. Once in the active cavity, a large initial increase in the phase signal was generated. As the water evacuated the active cavity, however, the signal should show a remaining offset generated by the presence of the optical fiber. Figure 7 shows one signal generated during this experiment.

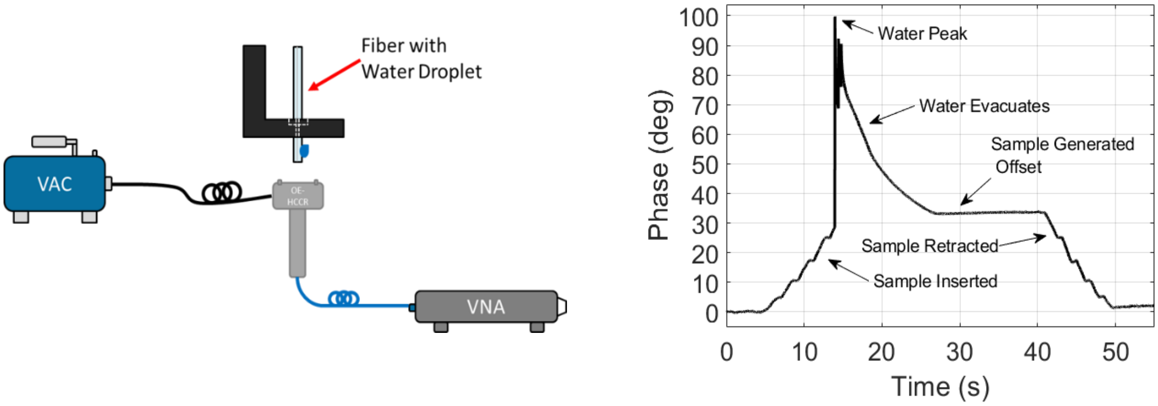

(a) (b)

Figure 5: Water droplet generated phase signal offset. (a) Secondary experimental setup for the simulation of the phase signal offset generated by a nonvolatile material present in the active cavity. Here, a fiber with attached water droplet was inserted into the probe. The fiber (the nonvolatile, analogous for droplets in breath) and the water droplet (the volatile, analogous for the volatile gasses in breath) simulate a more convincing scenario where all material enters the active cavity at roughly the same point in time. (b) Sharp rise and gradual fall of the signal due to the exposure and subsequent evacuation of a volatile compound (water), leaving the residual offset phase signal generated by the nonvolatile material (optical fiber).

As demonstrated in Figure 5, phase increased significantly as the wetted fiber entered the active cavity. Once the water had evaporated, the phase signal settles to a value offset from zero. As the fiber exited the active cavity, the phase signal returns to zero. Noticeable, there are some small step-like features in the signal as the fiber extends into or retracts from the active cavity. This is caused by the adjustment of the micromanipulator used to control the fiber's vertical position, which requires the experimenter to manually twist and then readjust. Each flat region in this step buildup occurs as the experimenter readjusts their grip on the micrometer.

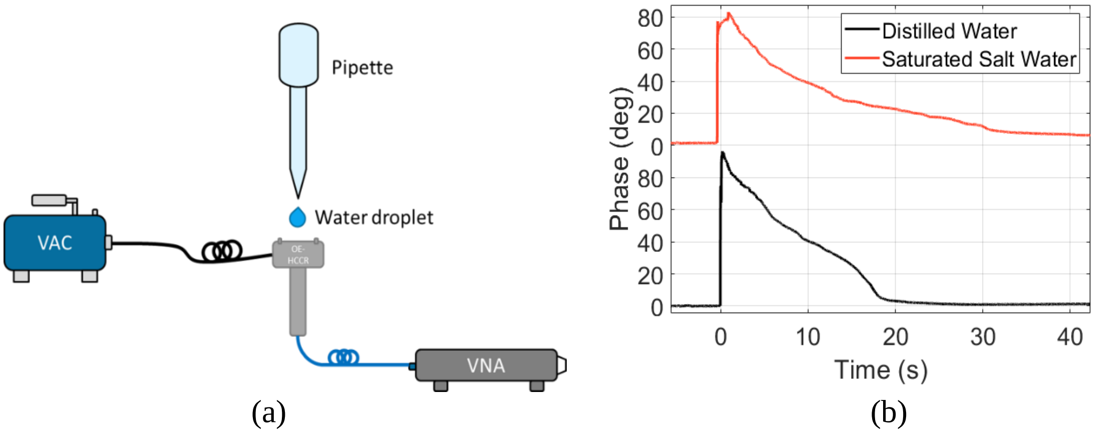

(a) (b)

Figure 6: Elongation of phase signal from nonvolatile particle immersion. (a) Final experimental setup for the simulation of the phase signal offset generated by a nonvolatile material present in the active cavity. Here, two solutions of water were inserted into the active cavity. First, pure distilled water was inserted into the cavity and the phase signal was collected. Then, saturated salt water was inserted into the active cavity and the phase signal was measured. The nonvolatile material, salt in this case, was to be analogous to the respiratory droplets in exhaled human breath. (b) Elongation of the phase response caused due to increased concentration of nonvolatile particulates. Here, five microliters of distilled water (control) and saturated salt water (test) were inserted into the active cavity in separate trials. The concentration of salt caused an elongation of the offset phase signal, leading to a slower descent from peak phase offset.

To simulate a phase signal more analogous to that of exhaled breath, one last experiment examined the signal generated by a combination of volatile and nonvolatile materials using a known volume of saturated salt water.

Figure 6 shows the phase signal generated by the droplet of saturated salt water. Here, there is an elongated return to the initial phase value, henceforth referred to as the “tail” of the signal. Through several trials, signals generated with saturated salt water consistently had a longer tail than signals generated with distilled water.

## 4.2. DEEP BREATHING VS. AMBIENT AIR

Thus far, all experiments have used mixtures of solid and/or liquid materials as a means of simulating complex mixtures of volatile and nonvolatile materials in the gas phase. To further support our proposed breath analyzer, it is imperative to extend the experimentation and verify that similar signals can be generated by filling the active cavity with gaseous materials. Further experimentation was necessary to confirm that any generated phase signal was due to the exhaled breath being directed into the active cavity rather than from some other phenomena affecting the OE-HCCR. The distinction between the proposed breath analyzer and a traditional means of measuring expired and inspired flow rates of human breath (e.g., spirometry) is our breath analyzer’s unique modality to characterize lung function: the OE-HCCR breath analyzer measures the variation of materials and their abundance rather than the influx of flow. However, our breath analyzer is capable of indirectly measuring flow through the analysis of the rate of modification of materials inside the active cavity. Thus, to establish the breath analyzer’s dependence on matter detection rather than direct flow, a simple experiment was constructed. First, a handheld air pump was used to direct a flow of ambient air from the surrounding room into the active cavity at roughly the same velocity of an exhaled breath. Several exhaled breaths were directed into the same breath analyzer under the same conditions.

This experiment was conducted using the 6mm probe with the following vector network analyzer settings: CW sweeping type, 10,000 points, IF bandwidth of 100 Hz, and a power level of +10 dB. The CW frequency was 562 MHz, the resonance frequency of this breath analyzer.

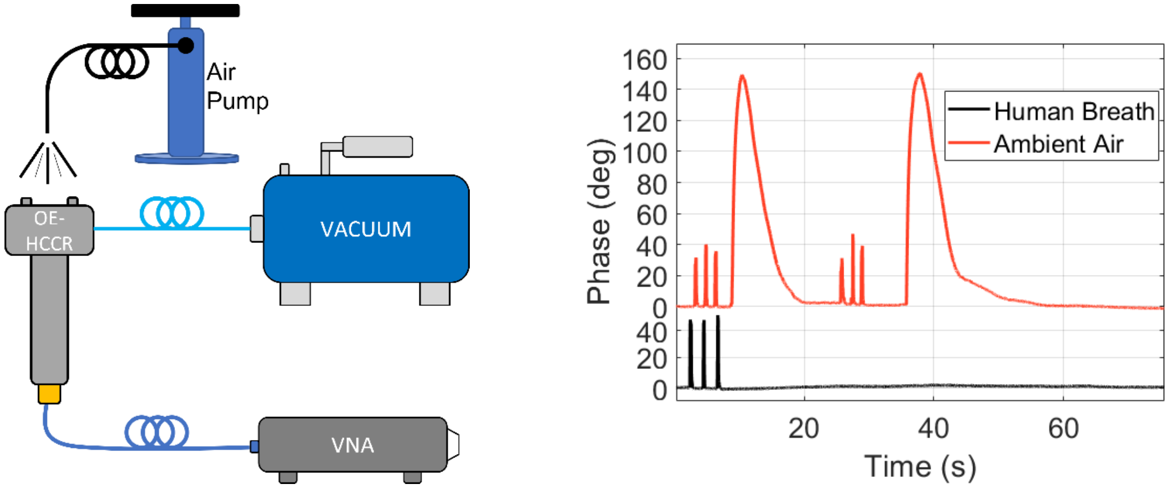

(a) (b)

Figure 7: Phase signal generated from similar flows of ambient air and human breath. (a) Experimental setup for the comparison of the phase signals generated by a flow of ambient air and an exhaled human breath. Separate sweeps were collected for both samples. First, an air pump would direct ambient air into the active cavity of the breath analyzer. Then, the experimenter would then direct an exhaled breath into the active cavity. Phase signals would be captured against time for both samples. (b) Comparison of signals generated by a direct flow of ambient air or exhaled human breath.

Figure 7 compares the generated signals from the two flows. While there are small phase drifts seen during the flow of ambient air into the active cavity, the generated change in phase signal is minimal when compared to those from human breath samples.

## 4.3. DIAPHRAGM SIMULATIONS OF PRESSURE FLUCTUATIONS IN AMBIENT AIR AND EXHALED HUMAN BREATH

To build upon the previous experiment, the comparison is repeated, this time capturing both the ambient air and the exhaled human breath into a diaphragm before flowing into the breath analyzer. The diaphragm is used to guarantee comparable flow and output volume of air, allowing for more controlled experimentation.

Five trials each of ambient air and exhaled breath were collected. In each trial, ambient temperature and atmospheric pressure were held constant. The breath analyzer was tuned to the same resonance frequency and power loss, swept at the same settings, and operated under a vacuum at a constant pressure of 20 torr. Each trial used the 2mm probe with a CW frequency of 4.243 GHz. Figure 8 compares the generated signals from the diaphragm filled with ambient air and the diaphragm filled with human breath.

Each trial began with three bursts of cleansing solution (DFE) directed into the active cavity, which are not shown in Figure 8 for simplicity’s sake. The similar magnitude of these DFE signal spikes strongly indicate similar sensitivity of the breath analyzer across both trials. Five seconds after the final burst of DFE, the diaphragm was deflated into the active cavity. The signal generated from human breath shows an additive phase with a duration of approximately seven seconds, after which the signal returned to its initial value, indicating the complete removal of volatile and nonvolatile materials from the active cavity and the return of ambient air. When the diaphragm of ambient air was deflated into the active cavity there was no such additive signal generated. Despite the contents of the active cavity being replaced in similar fashions for each trail, only trials flowing human breath into the cavity resulted in phase signal shift.

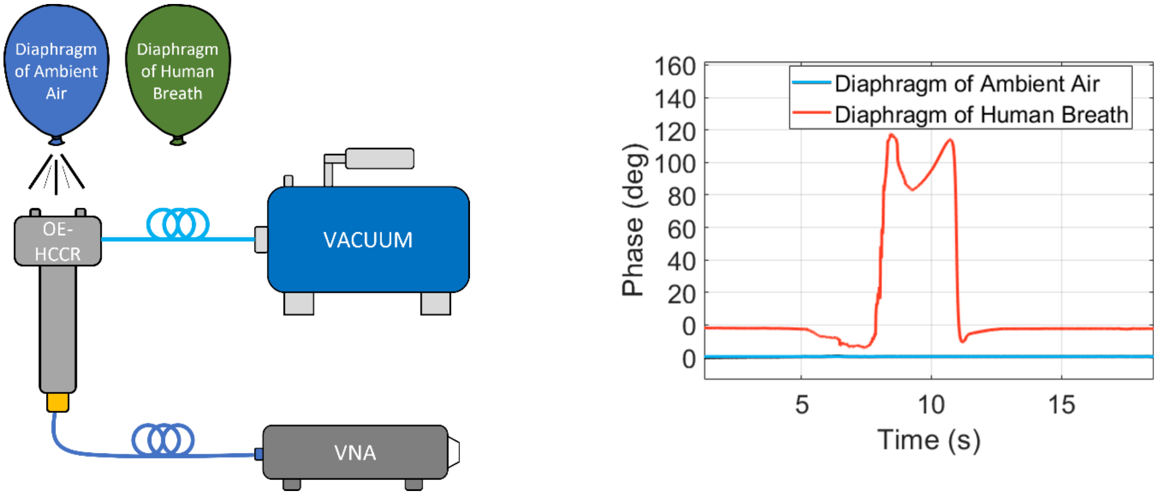

(a) (b)

Figure 8: Phase signal generated from diaphragms of ambient air and human breath. (a) Experimental setup for the comparison of phase signals generated by similar flow of ambient air and exhaled human breath. Here, one diaphragm each of ambient air (assumed to be of similar composition as the air already in the active cavity) and exhaled human breath were inserted into the active cavity in separate sweeps. (b) The signal response of the breath analyzer to a comparable flow rate of ambient air and human breath samples once released from diaphragm.

## 4.4. TIDAL VS. EXAGGERATED BREATHING

Next, experiments aimed to increase the amount of information collected per breath sample were conducted. To achieve this, an exaggerated breathing technique that uses the full vital capacity of an individual’s lungs was used. Doing so, we hoped to see an increase in the number of respiratory droplets per exhaled breath. This breathing style will be referred to as “exaggerated breathing”.

To best demonstrate the differences in the generated phase signals, three exhaled breaths were captures in the same sweep by the same individual. The first two breaths employed the exaggerated breathing style. For the third exhalation, the participant breathed tidally. This experiment was conducted with the 6mm probe at a CW frequency of 562 MHz.

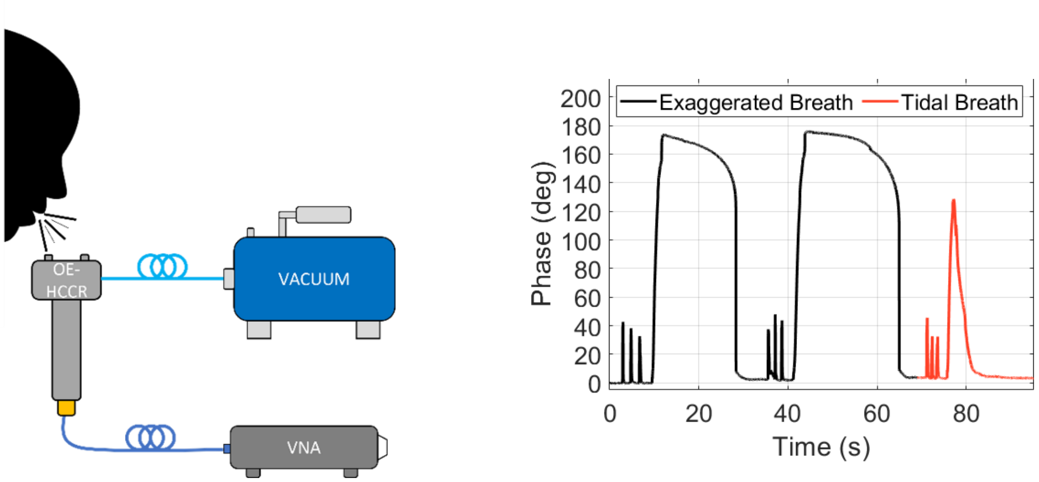

(a) (b)

Figure 9: (a) Phase signal generated from tidal and exaggerated breathing patterns. Experimental setup for the determination of breath schemes that produce greater amounts of respiratory droplets per breath. Here, two breathing techniques were compared. First, a proposed exaggerated breathing technique, which employs the full vital capacity of an individual's lungs, was used. This was then compared to a tidal breath. (b) Signal response of the breath analyzer to two stimuli separated by bursts of cleansing solution (DFE). From left to right: (1) two exaggerated exhalations of breath directed into the active cavity; (2) one tidal breath exhalation directed into the active cavity.

Figure 9 demonstrates the different phase signal responses of the breath analyzer to three stimuli: (1) three bursts of DFE to show similar sensitivity across trials; (2) two exaggerated exhalations of breath directed into the active cavity; and (3) a tidal breath directed into the active cavity. Here, the exaggerated breathing generates a phase signal that is approximately ten seconds in duration, compared to the four second duration signal from the tidal breath. Importantly, the magnitude of the phase shift is also greater for the exaggerated breathing technique, resulting in a better signal-to-noise ratio (SNR).

## 4.5. COMPARISON OF SEVERAL BREATHS FROM UNIQUE INDIVIDUALS

The next step was to utilize this finding among several individuals. Although a large-scale study among individuals is pending, we were able to collect several breath samples from four researchers in the Lightwave Technology Laboratory. Figure 9 shows the generated signal in response to these four individuals over several trials. Parameters under which these breath samples were collected were held constant. This experiment utilized the 6mm probe at a CW frequency of 562 MHz.

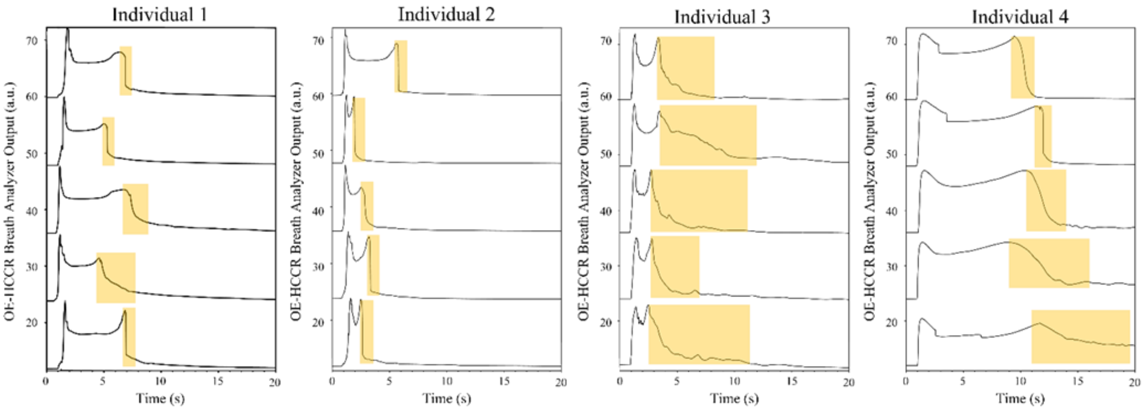

(a) (b) (c) (d)

Figure 10: Generated phase signals from five breath trials of four individuals employing an exaggerated breathing technique. Here, individuals 1 and 2 had no symptoms indicative of infection. Individuals 3 and 4, however, displayed symptoms of allergies, likely resulting in more exhaled respiratory droplets. The elongation of the phase signal's tail in individuals 3 and 4 is attributed to higher concentrations of exhaled respiratory droplets.

Several common features are seen across the samples collected by each individual. First, there is an evident immediate peak as the breath enters the active cavity, followed by a settling period and second peak. Importantly, there is a noticeably elongated tail on the phase signals generated by individuals three and four. Factors contributing to this will be reviewed in the discussion.

# 5. DISCUSSION

The OE-HCCR breath analyzer aims to distinguish healthy and compromised lung function through the quantification and assessment of nonvolatile materials in an exhaled human breath. The volatile nature of those compounds in human breath excluding respiratory droplets allows for their sudden evacuation of the active cavity, resulting in a return to the ambient relative permittivity, and thus, phase level seen in the generated signal. Importantly, theory dictates that a signal offset generated by particulates that do not easily exit the active cavity should remain. The first experiment demonstrates the stubborn nature of nonvolatile particulates (an optical fiber in this case) within the active cavity of the breath analyzer. Here, the signal offset is present until the fiber is removed. The nonvolatile of this experiment, DFE, demonstrates the expected signal masking caused by volatile materials with high permittivity. A similar signal pattern is expected in the case of human breath. The volatile compounds i.e., water, nitrogen, etc.) cause a large initial phase increase which masks the signal offset caused by the nonvolatile particulates exhaled in breath due to their substantially higher primitivities. However, once these volatile materials have evacuated the active cavity, whether through evaporation or due to the pull of the vacuum, the remaining nonvolatile particulates will generate a small offset from the initial phase value generated by the breath analyzer under constant pressure. The presence of this offset would be indicative of compromised lung function, as healthy breath should contain low enough concentrations of nonvolatile particulates to evade the OE-HCCR's limit of detection.

The first two experiments demonstrate the nature of volatile materials to quickly evacuate the active cavity, leaving only the residual nonvolatile materials that generate the offset phase signal. In the case of breath, we expect to see similar phenomenon, where the volatile materials in breath will quickly evaporate, leaving only the solid particulates that are indicative of compromised lung function. It should be noted that the vacuum will likely influence the small solid particulates as well, leading to their eventual, albeit slow, evacuation of the active cavity. This subtle clearing of nonvolatile and volatile materials alike can be seen in the third experiment. Here, saturated salt water inside the active cavity resulted in an elongated signal tail, likely due to the nonvolatile nature of the salt in the water which prevent the clean and quick evacuation of the active cavity. Furthermore, we expect that enhanced signal resolution would likely show the same step-like features as seen with the manual insertion and retraction of the optical fiber in experiments one and two, this time in smaller magnitude. Thus, we theorize that small amounts of salt are consistently being pulled out by the vacuum, causing this elongated tail feature in the signal. In later discussions, we will show that this same approach can be applied to the survey of exhaled breath. Here, the nonvolatile materials come in the form of respiratory droplets rather than salt, and the overall concentration of nonvolatiles is significantly smaller, but the elongation of the signal's tail is repeated.

The second set of experiments aimed to demonstrate our breath analyzer’s dependence on inhomogeneous materials and concentrations within its active cavity. Here, we found that the breath analyzer’s signal is largely unaffected by the flow of ambient air. This agrees with theory, which dictates that the breath analyzer will only generate varied signal when the effective permittivity inside the active cavity is modified or when the distance from the open end of the resonator to the attached facepiece is changed. Since the air in the active cavity initially had similar composition to the air in the surrounding room, and since the gap distance was held constant, no change in signal was generated. Further experimentation focuses on improving probe stability to mitigate the small fluctuations seen in the signal over several tens of seconds. Once long-term stability is achieved, the generated signal will not experience any changes since the composition of the flowed ambient air is the same as the air within the active cavity. Importantly, the signal did show significant variation in the case of exhaled breath.

With the second set of experiments demonstrating the breath analyzer’s ability to ignore background signal generated by the ambient environment, we repeated this observation, this time guaranteeing more sophisticated control of flow velocity and volume using two similar diaphragms filled with ambient air and exhaled human breath. Here, the generated signals were consistent with theory, demonstrating a shift in phase signal for exhaled human breath and a lack thereof for ambient air. This additive signal generated with human breath had a duration of approximately seven seconds before the signal returned to its initial value, indicating the complete removal of volatile and nonvolatile materials from the active cavity and the return of ambient air.

Due to the findings of experiment two and three, which supported the hypothesis that the breath analyzer measures breath content rather than flow, our fourth experiment aimed to generate more information per breath using an exaggerated breathing pattern. Here, we hoped that breathing with the full vital capacity of the lungs would produce more respiratory droplets containing nonvolatile particulates. This is directly in accordance with the current understanding of breath particulate generation as discussed previously. We found that our exaggerated breathing mechanism produced significantly longer signals, indicating a larger quantity of exhaled breath content per breath. We suspect this will prove important in future applications of this breath analyzer aimed at disease diagnosis, in which we will aim to measure concentrations of target organic compounds in breath for the determination of disease status.

In our last set of experiments, four researchers of the Lightwave Technology Laboratory were asked to breath into the breath analyzer using the exaggerated breathing technique. Here, each researcher captured five breath samples. Recall the elongated signal tails from the last two individuals. The signals generated by saturated salt water exhibited similar signal elongation. We theorize that the increased concentrations of nonvolatile materials in the samples elongated the tail of the phase signal in both experiments.

Depending on the amount of particulate matter in the breath sample and the depth of the exhaled breath, the additive signal can be elongated. Simply put, breaths that contain more nonvolatile matter will take longer to descend back to the initial phase value than a breath with very little nonvolatile particulates, which typically return to the initial phase

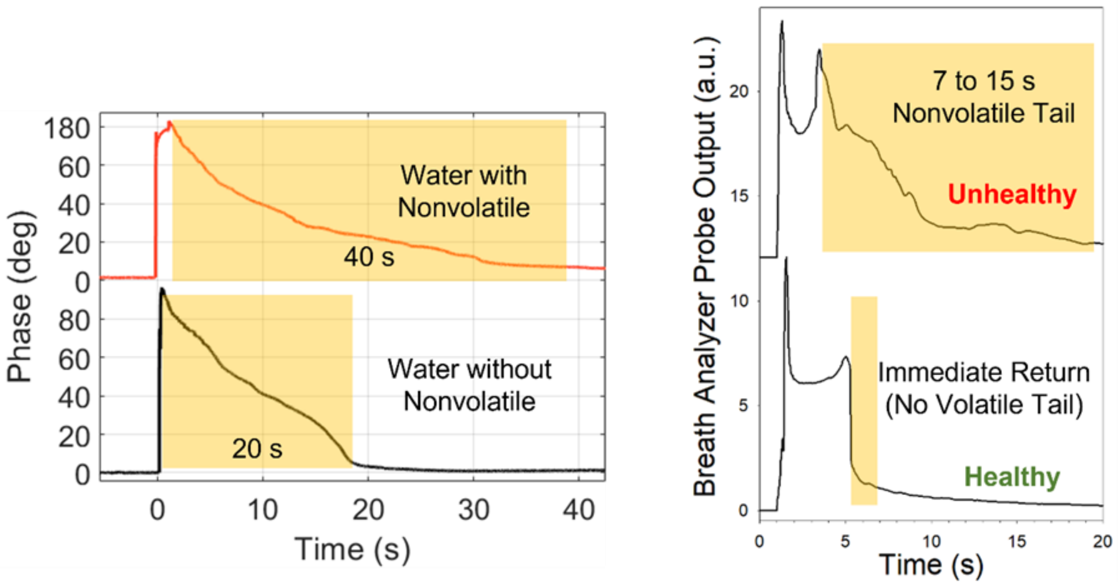

(a) (b)

Figure 11: Comparison between two sets of samples with varying concentrations of nonvolatile materials. On the left: the generated phase signal for two drops of water, one being distilled water and the other being saturated salt water. On the right: breath profiles from two individuals, one without allergies and one with allergies. Notice the similarities seen between the phase signals from distilled water on the left and individual 1 on the right. The signal returns relatively quickly to the initial phase value following the peak of the signal. Next, notice the similarities seen in the phase signals from saturated salt water on the left and individual 3 on the right. There is an evident tail on the phase signal, indicating a higher concentration of nonvolatile materials than in the corresponding control experiment.

value immediately following the second peak. Breath profiles with a present tail indicate the presence of particulates in the breath that do not quickly evaporate or evacuate the active cavity due to the presence of vacuum. In comparison, healthy breath will clear the chamber quickly due to its composition of water vapor and other volatile gases that quickly dissipate once within the active cavity. Breath that contains higher concentrations of nonvolatile materials, thus, will take longer to clear the active cavity, resulting in this tail following the second peak of the signal. Our preliminary experimentation supports that a signal that returns to less than 10% of its maximum value within one second following the second peak can be considered a breath with very minimal concentration of nonvolatile particulates. Importantly, both individuals three and four noted severe allergies during the time of this experiment. We suspect that the allergies increased the amount of matter in the exhaled breath of these two individuals, resulting in the elongated tail on their breath profiles. Furthermore, the longer tail seen in individual four's breath profiles would support that they were breathing out more particulates than any other individuals, indicating a more severe allergies than those had by individual three. Further experimentation with a larger sample size is underway to better support this interpretation.

## 6. CONCLUSION

We report a breath analyzer with ultra-high sensitivity and low limit of detection based on a novel technique — phase-shift-amplified microwave resonance — which can detect compromised lung function through measures of exhalation flow and breath content. The OE-HCCR serves as an inexpensive, robust, and highly sensitive breath analyzer that can be deployed as a preliminary means of testing for compromised lung function. The mathematical modeling of the breath analyzer was discussed in detail, demonstrating the theoretical capability of the OE-HCCR as a breath analyzer with high dynamic range and low limit of detection. Experiments support the hypothesis that volatile materials in breath (i.e., water vapor, nitrogen, etc.) will first dominate the phase signal generated by the breath analyzer. However, the volatile nature of these materials ensures that they quickly disperse, leaving only the offset signal generated by the nonvolatile particulates (i.e., virions) indicative of compromised lungs. Experimental results also verified that the breath analyzer is sensitive to exhaled breath flow and composition through two experiments, comparing tidal breathing to either ambient air from the surrounding environment or to an exaggerated breathing style employing full depletion of the lungs before a sharp inhalation and subsequent exhalation into the OE-HCCR. Furthermore, the breath analyzer was used to compare the breath signatures from four individuals, demonstrating the device’s capability of detecting differences between the exhaled breath of healthy and allergic individuals through changes in permittivity in the active cavity resulting from a modulation in the number of nonvolatile particulates in the breath. Most importantly, our results indicate that a typical breath sample will result in a 7 +/- 3 second modulation in the phase signal, mostly due to the increased presence of volatile materials inside the probe. Furthermore, breaths that generate signals with elongated tails, which we define as those that do not return to within 10% of the initial phase value in the first second following the second signal peak, are indicative of increased breath particulate concentration and thus of compromised lung function. The proposed breath analyzer is capable of distinguishing healthy and compromised individuals and could serve as a pre-diagnostic survey tool for compromised lung function. Thus, without any additional means of selectivity, the proposed OE-HCCR breath analyzer can be utilized to separate healthy and diseased individuals, allowing practitioners to quickly determine if a patient is ill and perform further diagnostic testing if necessary. Future work includes a prospective, real-world study in which the exhaled breath of 150 participants will be surveyed using two configurations of the OE-HCCR breath analyzer.

Although current experimentation focuses on the survey of nonvolatile materials in exhaled breath, further work is being conducted on the survey of volatile materials as well.

Future research aims to see the OE-HCCR breath analyzer have sufficient selectivity to diseases such as SARS-CoV-2 and kidney disease using thin-film metal organic framework (MOF) structures inside the active cavity. Through the modification of these materials, selectivity to key volatile organic compounds can be achieved. The concentrations of different panels of these organic compounds can then be monitored for the diagnosis of different pathogens and a determination of the level of contagion. The MOF structures should allow for proper capture of these volatile compounds without the dispersion effect seen with water in previous experiments. Exhaled breath volatiles can potentially provide similar insights into an individual's pulmonary function and disease state.

## 7. ACKNOWLEDGEMENTS

Research was sponsored by the National Institutes of Health as part of the RADx-rad program and was accomplished under grant award number 3U01HL152410-02S1. The views and conclusions contained in this document are those of the authors and should not be interpreted as representing the official policies, either expressed or implied, of the National Institutes of Health or the US Government. The US. Government is authorized to reproduce and distribute reprints for Government purposes notwithstanding any copyright notation hereon.

# SUPPLEMENTARY MATERIALS

## 1. INVESTIGATION OF THE LIMIT OF DETECTION FOR THE PROPOSED OE-HCCR BREATH ANALYZER

In early 2021, a prototype benchtop OE-HCCR breath analyzer probe was invented, fabricated, and tested to verify the ultrahigh sensitivity and low limit of detection. The key feature of the proposed OE-HCCR breath analyzer is the two-stage amplification scheme, which allows for resolutions that exceed nanometer scale common to advanced laser interferometer systems [30]. Here, we strive to further improve and optimize the OE-HCCR as an ultrasensitive breath analyzer probe. The OE-HCCR is formed by two electromagnetic (EM) wave reflectors in a hollow RF coaxial cable. These reflectors take the form of a metal post that connects the inner and outer conductors part way down the length of the OE-HCCR and the open end of the coaxial cable, as illustrated in Figure 4.

A porous metal plate is fitted to part of the OE-HCCR at a distance *d* away from the open end of the coaxial cable. The transverse EM wave mode in the OE-HCCR excites a fringing electric field at the end of the coaxial cable. Importantly, as the gap distance *d* decreases, the fringing electric field at the open end of the coaxial cable increases dramatically. Thus, the smaller the gap distance, the larger the electric field and the higher the sensitivity of the OE-HCCR to changes of dielectric properties within the medium of the active cavity formed between the open end of the coaxial cable and the metal plate.

The OE-HCCR can be mathematically described as an equivalent circuit. In this representation, the open end of the coaxial cable can be modeled simply as an effective capacitance that contains the fringing electric field. Importantly, the effective dielectric property of the active cavity is directly related to the capacitance. Employing spectral domain analysis, the capacitance is given by 1:

$$C = \epsilon_r \{ \frac{2\epsilon_0}{[ln(b/a)]^2} \int_a^b \int_a^b \int_0^\pi \frac{cos\phi' d\rho d\rho' d\phi'}{\sqrt{\rho^2 + \rho'^2 - 2\rho\rho' cos\phi'}} + \frac{4\epsilon_0}{[ln(b/a)]^2} \sum_{n=1}^{\infty} \int_a^b \int_a^b \int_0^\pi \frac{cos\phi' d\rho d\rho' d\phi'}{\sqrt{\rho^2 + \rho'^2 + 4n^2 d_1^2 - 2\rho\rho' cos\phi'}} \} \quad (A1)$$

where $a$ and $b$ represent the radial size parameters of the coaxial cable, $\epsilon_r$ and $\epsilon_0$ are the permittivities of the active cavity and vacuum, respectively. The capacitance sensitivity (i.e. the change in capacitance over change in dielectric constant of the active cavity), $\frac{\Delta C}{\Delta \epsilon_r}$, is a function of the gap distance *d*; the thinner the gap, the higher the capacitance and sensitivity. The phase reflection coefficient of the open end of the coaxial cable ($\phi_2$) and its dependence on the dielectric constant of the active cavity can be expressed as 2:

$$\phi_2 = -2tan^{-1}(2\pi f Z_0 C)$$

$$\Delta\phi_2 = \frac{4\pi f Z_0 1}{1 + 4\pi^2 f^2 Z_0^2 C^2} \frac{\Delta C}{\Delta \epsilon_r} \cdot \Delta\epsilon_r = M_1 \cdot \Delta\epsilon_r \quad (A2)$$

where $f$ is the interrogation microwave frequency and $Z_0$ denotes the characteristic impedance of the coaxial cable. $M_1$ denotes the coefficient, termed the first-stage dielectric sensitivity. According to equations 1 and 2, the dielectric property of the gap medium is directly encoded into the phase reflection coefficient of the open end of the coaxial cable. The inset in Figure 2b shows the dielectric sensitivity of $\phi_2$ (i.e. $M_1$) as a function of the gap distance *d*. Although an exponential increase in the dielectric sensitivity of $\phi_2$ is revealed as the gap distance $d$ decreases from 1 mm to 80 µm where the peak sensitivity reaches $5\ \times 10^{-5}$ deg/ppm, the sensitivity is not sufficient for the direct detection of virions in human breath.

To further improve the dielectric sensitivity and limit of detection (LOD) of the OE-HCCR, we propose a resonance-based amplification scheme inspired by the destructive interference-based phase-shift amplification in microwave-photonic interferometry [30], from which a thousand-fold amplification is expected. From the perspective of multiple reflectors (i.e., the EM wave reflecting back and forth in the cavity formed by two reflectors), the complex reflection coefficient $r$ of the microwave cavity resonator is derived as 3:

$$r = \frac{\Gamma_1 e^{-j\phi_2} - \Gamma_2 e^{j\phi_2} e^{-\alpha 2 d_0 - j\delta}}{1 - \Gamma_1 e^{j\phi_1} \Gamma_2 e^{j\phi_2} e^{-\alpha 2 d_0 - j\delta}} \tag{A3}$$

where $d_0$ is the cavity length, representing the physical distance between the metal post and the open end of the coaxial cable; $\delta = 4\pi d_0 f c$, denoting the round-trip phase delay due to the cavity length, $\alpha$ is the attenuation of the hollow coaxial cable, $\Gamma_1$ and $\Gamma_2$ are the magnitude reflection coefficients of the metal post and the open end of the coaxial cable, respectively; and $\phi_1$ is the phase reflection coefficient of the metal post. The phase term in the complex reflection coefficient can be derived as 4:

$$Pha = -tan^{-1}\frac{\Gamma_1 sin\phi_1 - \Gamma_2 e^{-\alpha 2d_0} sin(\delta - \phi_2)}{\Gamma_1 cos\phi_1 - \Gamma_2 e^{-\alpha 2d_0} cos(\delta - \phi_2)} + tan^{-1}\frac{\Gamma_1\Gamma_2 e^{-\alpha 2d_0} sin(\phi_1 + \phi_2 - \delta)}{1 - \Gamma_1\Gamma_2 e^{-\alpha 2d_0} cos(\phi_1 + \phi_2 - \delta)} \qquad (A4)$$

Using appropriate mathematical transformations and substituting the phase-matching condition of the resonator (i.e., $\delta - \phi_1 - \phi_2 = 2\pi + \theta$, with $\theta \approx 0$), into 4, we have:

$$\Delta Pha = \left(-\frac{\Gamma_1\Gamma_2 e^{-\alpha 2d_0}}{1-\Gamma_1\Gamma_2 e^{-\alpha 2d_0}} + \frac{\Gamma_2 e^{-\alpha 2d_0}}{\Gamma_1-\Gamma_2 e^{-\alpha 2d_0}}\right) \cdot (\Delta\delta - \Delta\phi_1 - \Delta\phi_2) \qquad \text{(A5)}$$

where $\Delta Pha$, $\Delta\phi_1$, $\Delta\phi_2$, and $\Delta\delta$ represent the change in $Pha$, $\phi_1$, $\phi_2$, and $\delta$, respectively. Since the variations of the dielectric property of the active cavity only contribute to changes in $\phi_2$, 4 can be rewritten as 6:

$$\Delta Pha = \left(\frac{\Gamma_1\Gamma_2 e^{-\alpha 2d_0}}{1-\Gamma_1\Gamma_2 e^{-\alpha 2d_0}}\right) \cdot \Delta\phi_2 = M_2 \cdot \Delta\phi_2 \qquad \text{(A6)}$$

where $M_2$ denotes the phase amplification coefficient, termed the second-stage phase-shift amplification factor. Equation 6 demonstrates how the change in phase reflection coefficient of the OE-HCCR at the resonance frequency (corresponding to the phase-matching condition) is magnified by $M_2$ compared to the change in the phase coefficient of the open end of the coaxial cable, $\phi_2$. Importantly, the smaller the difference between $\Gamma_1$ and $\Gamma_2 e^{-\alpha 2d_0}$ (i.e., the difference in magnitudes of the effective reflection coefficients of the first and second reflectors) the larger the amplification factor, which reveals the fundamental basis of the resonance-based phase-shift amplification response.

# REFERENCES

[1] T. A. Barnes and L. Fromer, “Spirometry use: Detection of chronic obstructive pulmonary disease in the primary care setting,” *Clinical Interventions in Aging*, vol. 6, no. 1. pp. 47–52, 2011. doi: 10.2147/CIA.S15164.

[2] M. R. Miller *et al.*, “General considerations for lung function testing,” *European Respiratory Journal*, vol. 26, no. 1, pp. 153–161, Jul. 2005, doi: 10.1183/09031936.05.00034505.

[3] V. C. Moore, “Spirometry: Step by step,” *Breathe*, vol. 8, no. 3, pp. 233–240, 2012, doi: 10.1183/20734735.0021711.

[4] S. R. Patel *et al.*, “The Role of Open-Lung Biopsy in ARDS*,” 2004. [Online]. Available: www.chestjournal.org

[5] W. J. Heerink, G. H. de Bock, G. J. de Jonge, H. J. M. Groen, R. Vliegenthart, and M. Oudkerk, “Complication rates of CT-guided transthoracic lung biopsy: meta-analysis,” *Eur Radiol*, vol. 27, no. 1, pp. 138–148, Jan. 2017, doi: 10.1007/s00330-016-4357-8.

[6] S. Haroon, P. Adab, R. D. Riley, D. Fitzmaurice, and R. E. Jordan, “Predicting risk of undiagnosed COPD: Development and validation of the TargetCOPD score,” *European Respiratory Journal*, vol. 49, no. 6, Jun. 2017, doi: 10.1183/13993003.02191-2016.

[7] J. Zhang, J. B. Zhou, X. F. Lin, Q. Wang, C. X. Bai, and Q. Y. Hong, “Prevalence of undiagnosed and undertreated chronic obstructive pulmonary disease in lung cancer population,” *Respirology*, vol. 18, no. 2, pp. 297–302, Feb. 2013, doi: 10.1111/j.1440-1843.2012.02282.x.

[8] P. M. Spieth and H. Zhang, “Analyzing lung crackle sounds: stethoscopes and beyond,” *Intensive Care Med*, vol. 37, no. 8, pp. 1238–1239, Aug. 2011, doi: 10.1007/s00134-011-2292-3.

[9] P. H. Quanjer *et al.*, “Multi-ethnic reference values for spirometry for the 3-95-yr age range: The global lung function 2012 equations,” *European Respiratory Journal*, vol. 40, no. 6, pp. 1324–1343, Dec. 2012, doi: 10.1183/09031936.00080312.

[10] S. Bickel, J. Popler, B. Lesnick, and N. Eid, “Impulse oscillometry: Interpretation and practical applications,” *Chest*, vol. 146, no. 3, pp. 841–847, Sep. 2014, doi: 10.1378/chest.13-1875.

[11] C. Massaroni *et al.*, “Optoelectronic Plethysmography in Clinical Practice and Research: A Review,” *Respiration*, vol. 93, no. 5. S. Karger AG, pp. 339–354, Apr. 01, 2017. doi: 10.1159/000462916.

[12] B. A. Simon, “NON-INVASIVE IMAGING OF REGIONAL LUNG FUNCTION USING X-RAY COMPUTED TOMOGRAPHY,” 2000.

[13] L. G. Dalbak, J. Straand, and H. Melbye, “Should pulse oximetry be included in GPs assessment of patients with obstructive lung disease?,” *Scand J Prim Health Care*, vol. 33, no. 4, pp. 305–310, Oct. 2015, doi: 10.3109/02813432.2015.1117283.

[14] T. A. Barnes and L. Fromer, “Spirometry use: Detection of chronic obstructive pulmonary disease in the primary care setting,” *Clinical Interventions in Aging*, vol. 6, no. 1. pp. 47–52, 2011. doi: 10.2147/CIA.S15164.

[15] W. Hamilton, T. J. Peters, A. Round, and D. Sharp, “What are the clinical features of lung cancer before the diagnosis is made? A population based case-control study,” *Thorax*, vol. 60, no. 12, pp. 1059–1065, Dec. 2005, doi: 10.1136/thx.2005.045880.

[16] A. Schneider *et al.*, “Diagnostic accuracy of spirometry in primary care,” *BMC Pulm Med*, vol. 9, Jul. 2009, doi: 10.1186/1471-2466-9-31.

[17] M. Kołodziej, M. J. de Veer, M. Cholewa, G. F. Egan, and B. R. Thompson, “Lung function imaging methods in Cystic Fibrosis pulmonary disease,” *Respiratory Research*, vol. 18, no. 1. BioMed Central Ltd., May 17, 2017. doi: 10.1186/s12931-017-0578-x.

[18] R. Ortega, C. J. Hmeansen, K. Elterman, and A. Woo, “videos in clinical medicine Pulse Oximetry,” 2011.

[19] Z.-C. Yuan and B. Hu, “Mass Spectrometry-Based Human Breath Analysis: Towards COVID-19 Diagnosis and Research.,” *J Anal Test*, vol. 5, no. 4, pp. 287–297, 2021, doi: 10.1007/s41664-021-00194-9.

[20] M. Malik, A.-C. Kunze, T. Bahmer, S. Herget-Rosenthal, and T. Kunze, “SARS-CoV-2: Viral Loads of Exhaled Breath and Oronasopharyngeal Specimens in Hospitalized Patients with COVID-19,” *International Journal of Infectious Diseases*, vol. 110, pp. 105–110, Sep. 2021, doi: 10.1016/j.ijid.2021.07.012.

[21] M. Zhou and J. Zou, “A dynamical overview of droplets in the transmission of respiratory infectious diseases,” *Physics of Fluids*, vol. 33, no. 3. American Institute of Physics Inc., Mar. 01, 2021. doi: 10.1063/5.0039487.

[22] J. Wei and Y. Li, “Airborne spread of infectious agents in the indoor environment,” *Am J Infect Control*, vol. 44, no. 9, pp. S102–S108, Sep. 2016, doi: 10.1016/j.ajic.2016.06.003.

[23] L. Morawska, “Droplet fate in indoor environments, or can we prevent the spread of infection?,” *Indoor Air*, vol. 16, no. 5, pp. 335–347, Oct. 2006, doi: 10.1111/j.1600-0668.2006.00432.x.

[24] R. Mittal, R. Ni, and J.-H. Seo, “The flow physics of COVID-19,” *J Fluid Mech*, vol. 894, p. F2, Jul. 2020, doi: 10.1017/jfm.2020.330.

[25] G. R. Johnson and L. Morawska, “The Mechanism of Breath Aerosol Formation,” *J Aerosol Med Pulm Drug Deliv*, vol. 22, no. 3, pp. 229–237, Sep. 2009, doi: 10.1089/jamp.2008.0720.

[26] M. J. Oldham and O. R. Moss, “Pores of Kohn: forgotten alveolar structures and potential source of aerosols in exhaled breath,” *J Breath Res*, vol. 13, no. 2, p. 021003, Mar. 2019, doi: 10.1088/1752-7163/ab0524.

[27] A. Wanner, M. Salathé, and T. G. O’Riordan, “Mucociliary clearance in the airways.,” *Am J Respir Crit Care Med*, vol. 154, no. 6, pp. 1868–1902, Dec. 1996, doi: 10.1164/ajrccm.154.6.8970383.

[28] J. Gralton, E. Tovey, M.-L. McLaws, and W. D. Rawlinson, “The role of particle size in aerosolised pathogen transmission: a review.,” *J Infect*, vol. 62, no. 1, pp. 1–13, Jan. 2011, doi: 10.1016/j.jinf.2010.11.010.

[29] E. L. Anderson, P. Turnham, J. R. Griffin, and C. C. Clarke, “Consideration of the Aerosol Transmission for COVID-19 and Public Health,” *Risk Analysis*, vol. 40, no. 5, pp. 902–907, May 2020, doi: 10.1111/risa.13500.

[30] C. Zhu, R. E. Gerald, Y. Chen, and J. Huang, “Probing the Theoretical Ultimate Limit of Coaxial Cable Sensing: Measuring Nanometer-Scale Displacements,” *IEEE Trans Microw Theory Tech*, vol. 68, no. 2, pp. 816–823, Feb. 2020, doi: 10.1109/TMTT.2019.2951099.

[31] S. Fan, K. Staebell, and D. Misra, “Static analysis of an open-ended coaxial line terminated by layered media,” *IEEE Trans Instrum Meas*, vol. 39, no. 2, pp. 435–437, Apr. 1990, doi: 10.1109/19.52531.

# SECTION

## 4. IDENTIFICATION OF BREATH TRANSIENT FEATURES OF INTEREST THROUGH A N=150 PARTICIPANTS STUDY OF EXHALED BREATH

### 4.1. MOTIVATION

Following the discussion of the previous paper, we hypothesized that a larger sample size would offer more fidelity in our analysis of breath transient signals. To do such, we set out to conduct an IRB-approved study in which several breath transient signals would be collected from a wider population of participants. In early 2022, our biomedical study, entitled “Preliminary Non-Invasive Human Breath Tests to Identify Baseline of a Field Deployable Novel COVID-19 Detector”, was approved by the institutional review board, being granted project number 2065704.

### 4.2. PARTICIPANT SELECTION

As part of our IRB-approved study, we are allowed to conduct up to six breath tests each from 150 individuals. Strict inclusion and exclusion criteria were established to guarantee maintained ethics throughout the study. All participants must be (1) 18 years of age or greater and (2) able to provide informed consent. Further, an individual was to be excluded from the study if the following criteria were met: (1) unable to provide informed consent: (2) unable to undergo randomization; and (3) the individual was previously or currently diagnosed with a breathing disorder (i.e., asthma, COPD, apnea, etc.).

Each participant was offered compensation in the form of a $5 amazon gift card for their participation in our study. Further, to protect any sensitive information, each participant was assigned a randomized five-digit number that would be used to identify their breath transients.

As of November 29th, 2022, 22 participants have engaged with our study. Recruitment efforts included posting flyers in common areas and speaking to undergraduate courses with the instructor's consent. With the 22 current participants, nearly 100 breath transients have been collected.

## 4.3. METHODS

The study takes place in one of two locations depending on reservations and traffic. These two locations are the first-floor lobby of the Emerson Electric Company Hall and the second floor of the Curtis Wilson Laws Library. Participants are greeted by the researcher and brought into a private area of the one of the above study locations where they are in a high-back chair with arm rests in front of a table. The researcher then gives a brief overview of the study protocol and allows the participant to ask questions about the study. The participants are asked to read and sign an informed consent form. Once the consent form has been properly filled out, the researcher prepares the OE-HCCR in front of the participant. The settings of the vector network analyzer (VNA) are set such that 100 seconds of breath data will be collected to allow for ample time for the signal to recover to the baseline. Once the participant is ready, the researcher expels three bursts of cleansing solution (difluoroethane) into the probe and then allows the participant to expel one full breath (approximately four seconds) into the probe. If sufficient data is collected, meaning that the network analyzer indicated an influx of material and that there is a continuous measurement of matter inside the probe, the researcher saves the data, resets the probe, and begins training the participant on the breathing procedure for the second phase of data collection. If sufficient data is not collected, the participant is asked to repeat the previous step after the researcher has reset the probe as needed. The second phase of data collection requires that the participant breathes in an exaggerated, quick manner. The researcher trains the participant on the proper breathing technique for the second phase of data collection and then, when the participant is deemed ready, sets the probe to collect another 100 seconds of data. The researcher once again expels three bursts of cleaning solution into the probe, which is followed by the participant's exaggerated breath (approximately four seconds). Again, if the probe does not properly collect all the data, the participant will be asked to repeat this second phase until proper data has been collected, each time with the researcher resetting and cleansing the probe as necessary. If the previous two breath trials have not exceeded fifteen minutes in combined length, the participant is asked to repeat this process until the fifteen minutes is complete. Once time is up, the participant is given the compensation as described above and will be allowed to leave. The researcher remains available for any questions that participants might have. The probe and all surrounding surfaces are cleansed using disinfectant and the network analyzer software is reset.

### 4.4. RESULTS

Nearly 100 breath transient signals have been collected from the 22 participants as of November 29th, 2022. For the sake of concise reporting, select breath transients have been overlayed in Figure 4.1. The rising edges of each breath have been aligned to demonstrate the variable length of the phase signal offset.

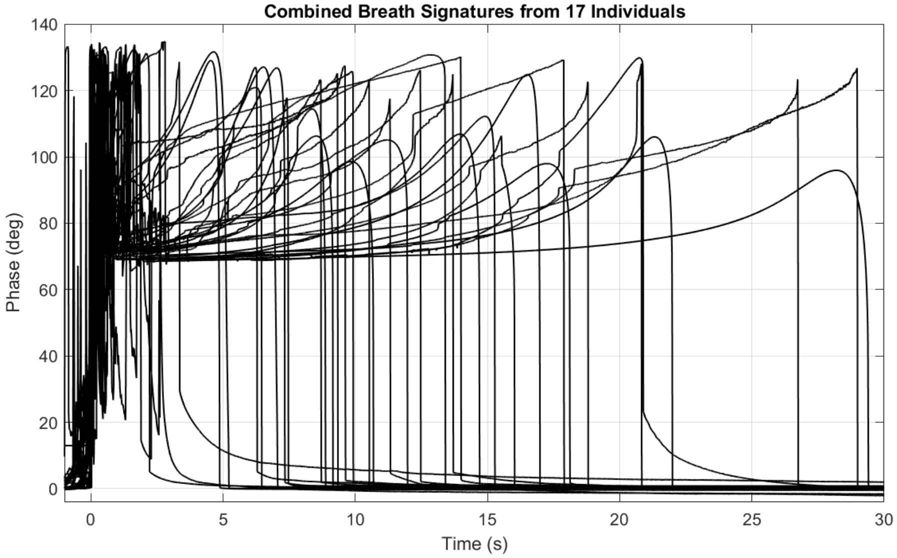

Figure 4.1: Breath transient signals from 17 individuals. Selected breath transient signals collected as part of the N=150 participants exhaled breath study are shown to demonstrate the consistent features of each.

### 4.5. DISCUSSION

The results of the larger sample size collected in our IRB-approved study further suggest the existence of several common features amongst each breath transient signal. Further analysis of these features allows for more in-depth interpretation of the breath profiles. Notably, each breath transient can be separated into three distinct regions, with the transition between regions being the respective relative maximum phase peak.

Furthermore, insight into the phase response in relation to probe coupling has allowed for a deeper interpretation of the maximum peaks, allowing for a greater understanding of the falling edge of the breath transient signal in particular.

**4.5.1. Active Exhalation.** Our analysis of the breath transient signals begins with the rising edge of the signal, which we denote as the "active exhalation" region. Importantly, this region is the only region of the breath transient that occurs simultaneously to the exhalation of the participant. All subsequent features of the breath transients are a result of the digestion of aerosol and nonvolatiles inside the active cavity of the resonator due to the presence of a vacuum. Thus, since this region is the only one that meters an influx of materials rather independent of the concentration of nonvolatiles, it follows that there is a consistent phase curve throughout this region among all collected breath transients thus far. Figure 4.2 shows the common rising edge feature seen in the active exhalation region.

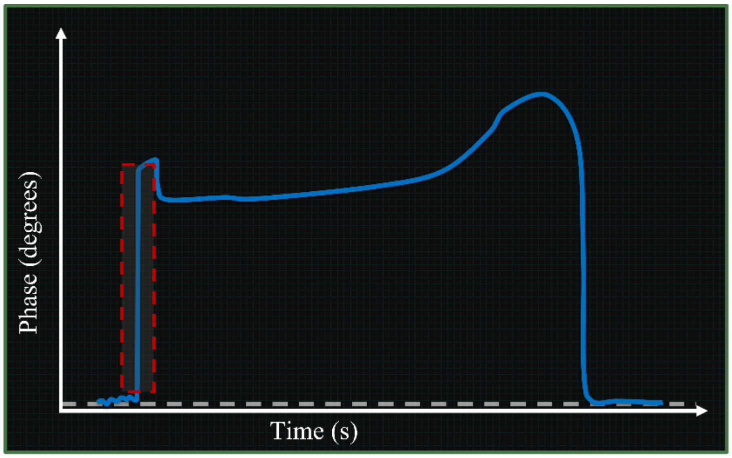

Figure 4.2: Active exhalation region of the breath transient. A single rising edge is consistent among all collected breath transient signals.

**4.5.2. First Phase.** Marking the transition between the active exhalation and aerosol digestion regions is the first phase peak. Here, the dramatic change in relative permittivity inside the active cavity has caused the phase curve to shift to frequencies significantly lower than the original resonance frequency, causing the peak of the phase curve to surpass the CW frequency. Across all breath transients thus collected, two distinct patterns for the first phase peak have been identified. First, smooth features surrounding the phase peak signify a stable and consistent shift of the phase curve to lower frequencies. Alternatively, noisy features surrounding the first phase peak suggest instability in the phase curve as it passes through the CW frequency, likely due to variations in the rate of exhaled breath or a slight modification of the phase coupling of the probe. A change in the rate of exhalation could account for the noisy features surrounding the first peak due to an inconsistent influx of materials into the active cavity. The other and more likely possibility is that the phase curve experienced a slight modification in its amplitude due to changes in the resonators coupling condition. As breath enters the active cavity, the probe can approach critical coupling from an overcoupled state, resulting in a modulation of the phase curve’s amplitude. This phenomenon would likely result in instability of the phase curve, generating noise in the breath transient signal until stability is achieved once again. Figure 4.3 distinguishes the two features often seen following the first phase peak of the breath transient signal.

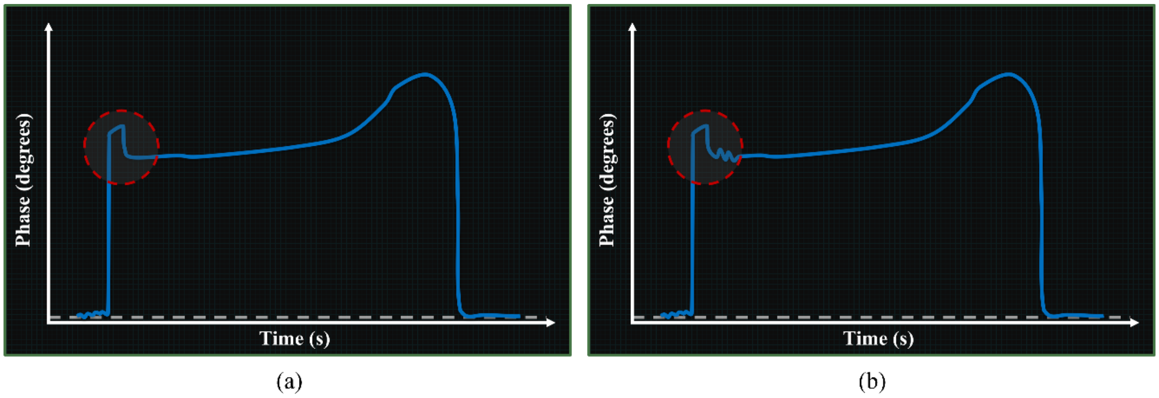

(a) (b)

Figure 4.3: First phase peak of the breath transient. Two common features of the breath transient signal following the first phase peak. (a) A smooth signal following the phase peak signifies a consistent shift in the phase curve across the CW frequency. (b) Noisy features following the first phase peak point to modulations of the phase curve as it passes across the CW frequency.

**4.5.3. Aerosol Digestion.** The second region of the breath transient response has been denoted as the "aerosol digestion" region. The aerosol digestion region is the longest in duration, spanning anywhere from three seconds to thirty seconds in length. Here, the breath transient signal meters the breakdown of the aerosol particles into volatile and nonvolatile gas components, allowing for the rapid evaporation of the volatile components. The effect of the remaining nonvolatiles will be discussed in sections 4.5.4 and 4.5.5. There are three distinct patterns that have been identified through the aerosol digestion region: smooth phase reversal, phase curve modulation, and a shelfed phase. Figure 4.4 demonstrates the different breath transient features that correspond to each pattern through the aerosol digestion region.

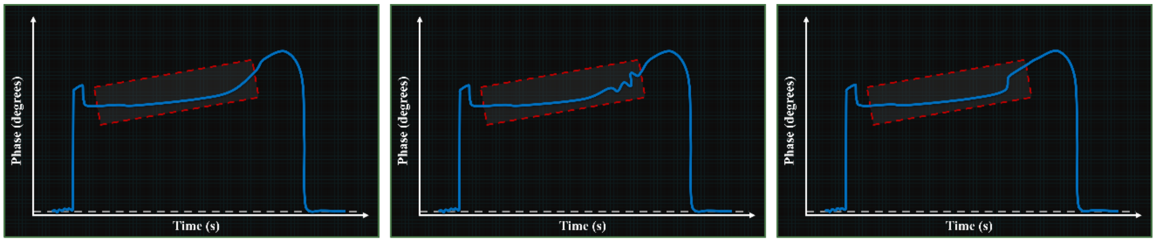

(a) (b) (c)

Figure 4.4: Aerosol digestion region of the breath transient. There are three distinct patterns that have been identified in the aerosol digestion region of the breath transient signal. (a) A smooth breath transient through the region suggests a smooth and consistent phase curve as it reverses in sweep direction and approaches the original resonance frequency. (b) Noise towards the end of the region points to a modulation of the phase curve amplitude as the sweeping direction reverses, causing similar noisy features to those seen following the first peak. (c) A steep slope that plateaus into a significantly shallower slope indicates a large amount of nonvolatile materials being purged from the active cavity by the vacuum over a short duration.

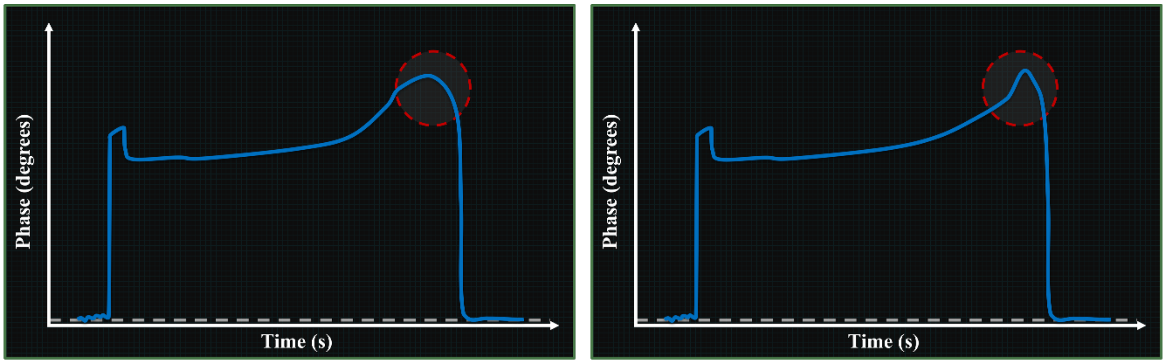

(a) (b)

Figure 4.5: Second phase peak of the breath transient. The second phase peak of the breath transient signal marks the instant the maximum amplitude of the phase curve crosses the CW frequency. Two distinct patterns offer insight into the nature of exhaled breath evaporation inside the active cavity. (a) A rounded peak hints at a consistent rate of evaporation among the contents of the active cavity. (b) A hooked peak indicates a nearly instantaneous evaporation of the materials inside the active cavity.

**4.5.4. Second Phase Peak.** The second phase peak marks the transition between the aerosol digestion and droplet evaporation regions of the breath transient signal. Here, the sweep direction is now reversed, meaning that the effective permittivity inside the active cavity is decreasing back towards that of ambient air, resulting in the phase curve to shift towards higher frequencies. The maximum level of the peak marks the instant the maximum amplitude of the phase curve crossed our selected CW frequency. Results indicate the pressence of two distinct patterns for the second phase peak. Figure 4.5 distinguishes the two patterns found across the breath transients collected thus far.

A rounded peak indicates the presence of nonvolatile particles inside the active cavity that allow the water content of breath to slowly dissipate in a consistent manner. Alternatively, a hooked peak indicates a quick evaporation of a large concentration of materials inside the active cavity. We theorize that this phenomenon is due to nonvolatile materials being dislodged from the surfaces inside the active cavity and being dissipated due to the vacuum. While the nonvolatiles themselves would not cause a significant change in permittivity that would be in accordance with the hooked nature of the second peak, the removal of the surrounding water particles that dissipate with the nonvolatiles could easily cause a large enough change in effective permittivity to account for the rapid variation in phase level.

**4.5.5. Droplet Evaporation.** The droplet evaporation region of the breath transient marks the return of the phase curve to a frequency approaching the original resonance frequency. This region often reveals the most direct evidence for identifying healthy and compromised lung functions. The evaporation region contains at least three distinct features of the region, identified thus far, that characterize the exhaled breath transient signal. Most common is a rapid falling edge in which the phase level quickly returns to its initial value. Here, the quick return to initial phase levels indicates an absence of nonvolatile particles in breath that would cause the water content of the breath to cling to the insides of the active cavity. This feature unambiguously identifies “healthy breath” and consists of a rapid drop in the probe phase (< 0.3 seconds) to the baseline at the termination of the exhaled breath transient. Next, a gradual falling edge of the breath transient signal indicates the presence of nonvolatile materials in the active cavity, causing a prolonged evacuation of the active cavity. These nonvolatile materials will cause the water content of breath to persist within the active cavity for a longer duration of time. Current results support the hypothesis that a shallower slope is indicative of an increased volume of nonvolatile materials inside the active cavity either due to an increased concentration of these materials or an increased nonvolatile particle size distribution. Lastly, an offset phase level following the falling edge of the breath transient indicates that some quantity of material resisted evacuation of the active cavity, resulting in a increased effective permittivity as compared to the initial level. Since the nonvolatile nature of breath aerosols would dictate their evaporation from the active cavity, it is theorized that this offset phase level is due to remaining nonvolatiles. The different features of the droplet evaporation region can be seen in Figure 4.6.

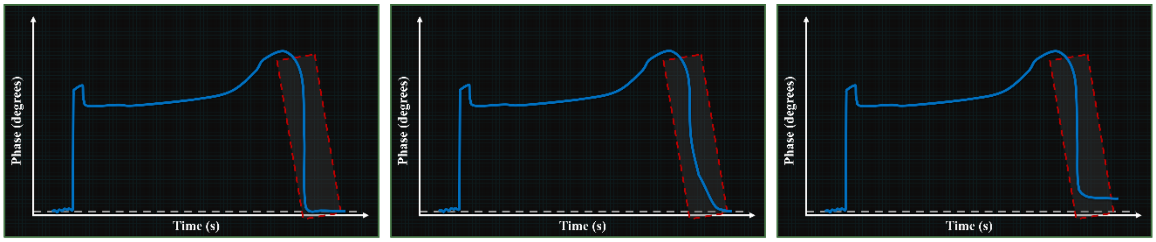

(a) (b) (c)

Figure 4.6: Droplet dissipation region of the breath transient. (a) A rapid falling edge feature indicates an absence of nonvolatiles in the exhaled breath. (b) A gradual falling edge feature suggests the water contents resistance to evacuation due to the presence of some nonvolatile exhaled particles. (c) An offset phase level is indicative of high amounts of nonvolatile particles in breath, suggesting compromised lung function.

# 5. OE-HCCR SIMULTANEOUS SENSING OF SOUND WAVES AND PERMITTIVITY FLUCTUATIONS TO SUPPLEMENT MACHINE LEARNING ALGORITHMS FOR THE DETECTION OF DISEASES THROUGH VOCAL BIOMARKERS

## 5.1. MOTIVATION

Several months into the COVID-19 pandemic, several studies suggested the efficacy of pre-screening individuals for the disease using smartphone-enabled artificial intelligence algorithms, alleviating the strain caused by test shortages and the economic repercussions of large-scale testing [6]–[9]. Most notably, MIT researchers were able to develop an AI model that could achieve a COVID-19 sensitivity of 98.5% for symptomatic individuals and 100% for asymptomatic individuals, when validated with an FDA approved COVID-19 test. Further, specificities for each group were 94.2% and 83.2%, respectively [9] Early adoption of this technology might have potentially produced a free, non-invasive, real-time, any-time, instantly distributable, and rapid large-scale deployable COVID-19 asymptomatic screening tool to anyone with access to a smartphone or personal computer with a microphone. Further, speech biomarkers may exist for many diseases, allowing for the development of similar models for a variety of diseases.

However, with a growing list of diseases identifiable by speech biomarkers, sensitivity and specificity of the AI models becomes a large concern. For the adoption of AI diagnostic models to be feasible, the sensitivity and specificity of each model must exceed those quantities generated by the accepted tests for each respective disease. With a growing list of diseases that can be marginally detected using AI models, the distinction between the different diseases gets blurred. Some vocal biomarkers can be presented due to a variety of diseases. Thus creates the need for a supplemental biomarker for tangential analysis. The coupling of multiple distinct biomarkers, collected via mobile sensors present on smartphones and other personal electronics, would allow for the identification of more complex diseases at higher sensitivities. Further, several studies report a relationship between the amount of expiratory aerosol particle emission and voice amplitude and individual spoken phenomes [10]–[12]. Here, we develop a supplemental microphonics technique that allows for the simultaneous collection of both sound and variations in airborne materials through the monitoring of mechanical vibrations and relative permittivity fluctuations. We aim to improve the selectivity and sensitivity of artificial intelligence models through the coupling of multiple biomarkers, offering preliminary experimentation for this claim.

## 5.2. METHODS AND RESULTS

To support our hypothesis that the two sensing techniques will provide two independent, tangential datasets, we constructed a simple experiment to showcase the analysis of unique parameters for each sensor, namely the monitoring of pressure waves by the microphone and the monitoring of exhaled matter by the OE-HCCR.

**5.2.1. Demonstrating The Independent Nature Of Two Sensing Techniques For Tangential Data Collection.** For this set of experiments, we opted to monitor the magnitude of reflected power at the resonance frequency rather than phase. This was done due to the variability of the phase signal at sub-gigahertz frequencies caused by the continuous variations in the probes coupling. In short, the phase signal is largely affected by the probe transitioning from overcoupled to undercoupled or vice versa, whereas the magnitude is relatively stable. Understanding this aim of differentiating the two signals, we first collected datasets for two combinations of input parameters: (1) creating pressure waves without causing fluctuations in the ambient concentrations of chemicals in air and (2) creating permittivity fluctuations with minimal creation of sound waves. Doing such, we expected to observe modifications in the corresponding signals and a constant state for the unaffected signal. For example, we expect to observe an obvious sound signal collected via the microphone and no modification of the phase signal of the OE-HCCR in the case of created pressure waves and no modification of the ambient air.

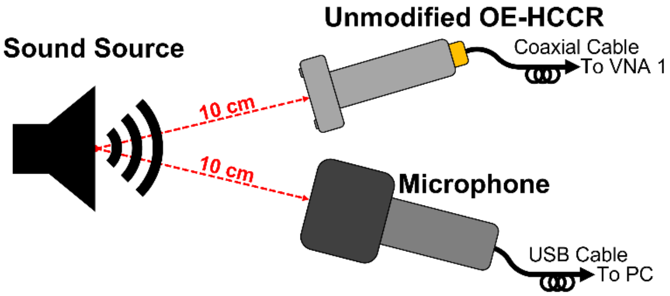

Figure 5.1: Experimental setup to demonstrate the independent nature of the OE-HCCR to sound. Here, we generate frequencies, allowing for the modification of the microphone's signal. However, since there is no modification of the ambient air, we expect the OE-HCCR to report a constant phase signal.

Figure 5.1 shows the experimental setup for our first experiment. Here, we arranged the OE-HCCR and microphone to face a speaker which generated several frequencies. Generating frequencies of 2 kHz, 10 kHz, and a random distribution of frequencies within this range, we were able to observe the response of the OE-HCCR to generated sound waves. Figure 5.2 shows the response of both sensors to the generated frequencies.

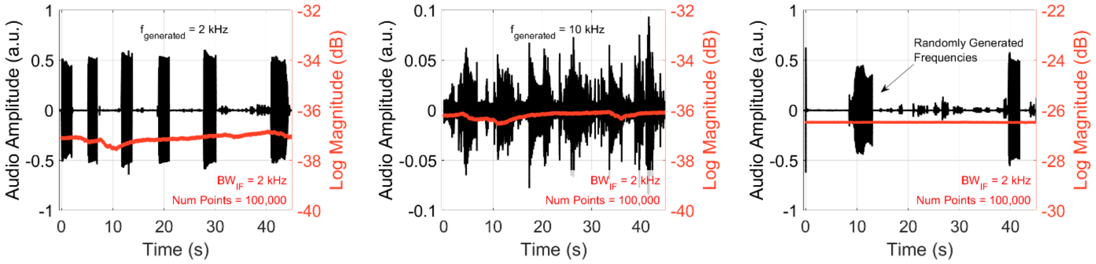

Figure 5.2: Various audio signals from two sensors. Audio and magnitude data collected via the microphone and OE-HCCR, respectively, to three different generated frequencies: (a) $F_{generated}$ = 2 kHz; (b) $F_{generated}$ = 10 kHz; and (c) randomly generated frequencies.

Notably, the OE-HCCR's generated signal remained within +/- 0.2 dB of its initial signal. This will be compared to the changes in signal magnitude in cases with varying permittivities later in the article. The implications of the IF bandwidth and number of points collected for the S11 signal of the OE-HCCR will be discussed further in the discussion.

Next, we aimed to isolate our focus on fluctuations of airborne material encountering the two sensors. To do so, we constructed a similar arrangement as seen in Figure 5.1, this time substituting the sound source with a permeating chemical source. An airflow directed between the two sensors will guarantee equal exposure to high concentrations of the permeant in air. Figure 5.3 shows the experimental setup.

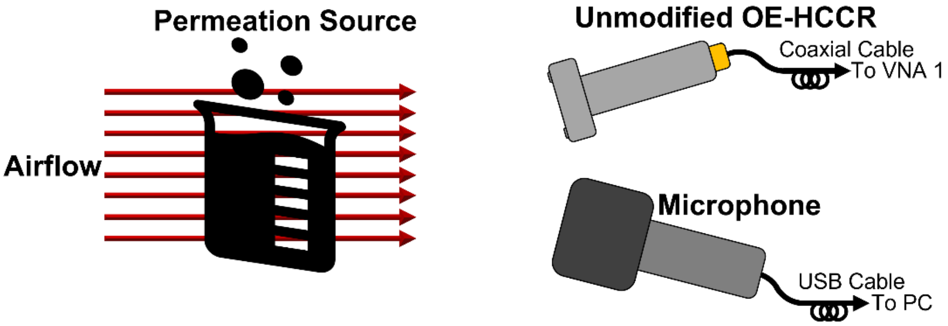

Figure 5.3: Experimental setup to demonstrate the independent nature of the microphone to permittivity fluctuations. Here, we generate airborne chemical concentrations with minimal noise (generated by the fan), allowing for the modification of the OE-HCCR's signal. Since there is minimal noise, we expect the microphone signal to remain constant.

It is important to note that the airflow was fan-generated, thus causing some small amount of noise that is present in the microphone signal. There is a noticeable phase buildup when the sensors were exposed to airborne permeant. We selected acetone as our permeant for this experiment, largely due to its high evaporation rate. Figure 5.4 shows the generated signals of the two sensors.

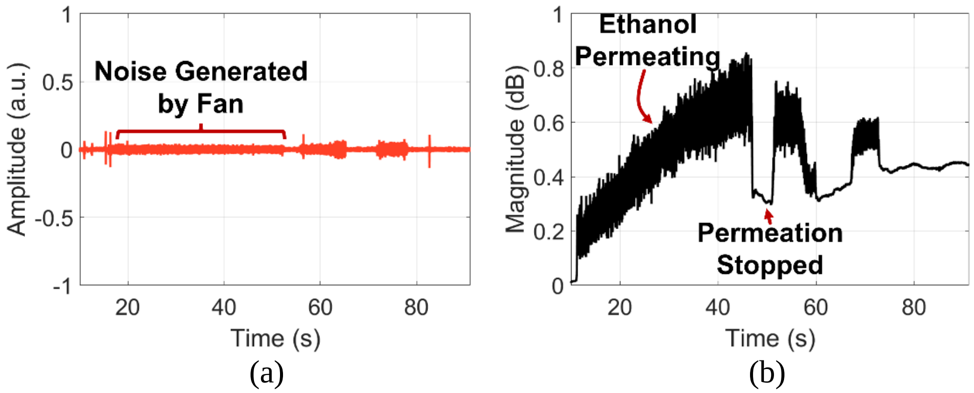

Figure 5.4: Permittivity signals collected by two sensors.. (a) The microphone signal shows slightly more noise than baseline during exposure to the permeant, likely attributed to the noise generated by the fan. (b) The OE-HCCR magnitude signal shows dramatic shifts in resonance frequency magnitude when exposed to permeant and a rapid return to baseline signal when not exposed.

### 5.2.1. Comparison Of Tangential Signals: Audio And Matter Collection Using A Two-Sensor System.

With the understanding that the two sensors are measuring parameters independent of one another, we aimed to demonstrate the tangential nature of the two signals obtained from microphonics and microwave resonance-based sensing. With the objective of providing supplemental data for the AI analyses of individual health through the monitoring of speech and forced cough patterns, we wanted to observe the similarities and differences in the features obtained through the two sensing technologies. To do such, we arranged a traditional microphone and an OE-HCCR equidistant from an individual who would repeatedly perform forced coughs and rapid exhalations. Assuming that the exhaled matter that would be measured by the OE-HCCR could propagate with the sound waves, we expected to see variations in the two signals at roughly the same time. The experimental setup for these trials can be seen in Figure 5.5.

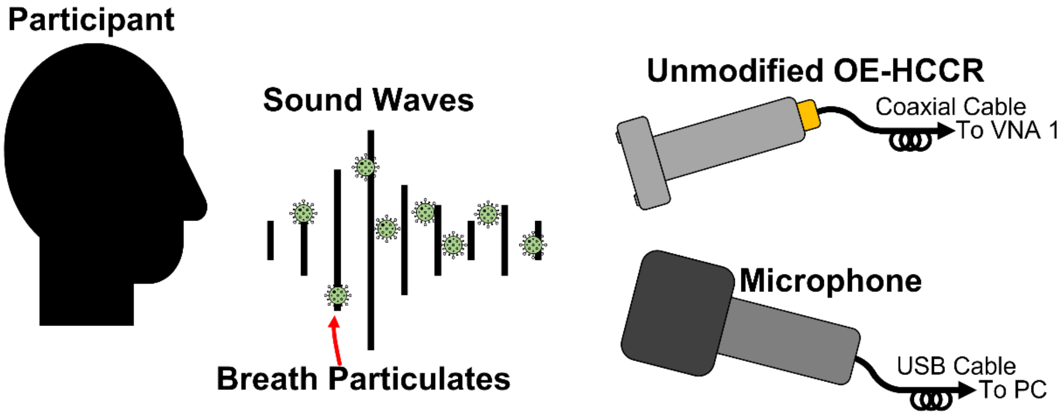

Figure 5.5: Experimental setup coupling sound and permittivity fluctuations with two sensors. This experimental setup aimed at demonstrating the tangential nature of two signals: the noise signal from the microphone and the log magnitude at the resonance frequency from the OE-HCCR.

Further, to demonstrate the OE-HCCR's dependence once again on permittivity changes to produce a dramatic change in magnitude at the resonance frequency, trials were also conducted in which the participant wore a surgical-grade mask to prevent the propagation of expiratory aerosol particles. Figure 5.6 demonstrates the difference in signal when the participant (a) performed a rapid expiration; (b) performed a forced cough; and (c) alternated wearing a mask and being maskless.

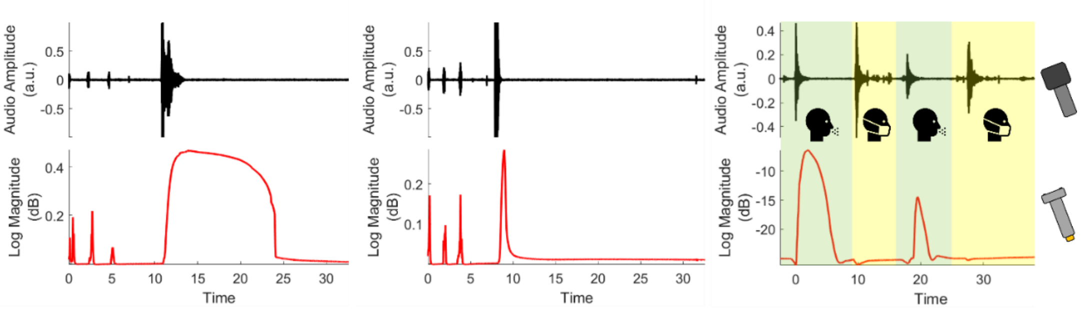

(a) (b) (c)

Figure 5.6: Sound and permittivity signals collected by two sensors. The resulting signals of the two sensors shown in black and red, being the audio signal and the log magnitude of the resonance respectively. (a) The sound and permittivity signals recorded when the participant performed a forced cough; (b) The sound and permittivity signals recorded when the participant performed a rapid exhalation; (c) demonstration of the dampened permittivity signal when the participant wore a surgical mask.

### 5.2.1. Microphonics Via A Modified OE-HCCR With Thin Metal-Film Diaphragm Facepiece.

With the experiments in section 5.2.2 aiming to demonstrate the tangential nature of the two sensors, one offering information collected via vocal biomarkers and the other offering insight into the material composition of the breath or speech carried by those same pressure waves, we aimed to determine whether a single sensor could collect the two datasets simultaneously. We selected the OE-HCCR for this experiment. Knowing that the resonance frequency of the probe's reflected signal (S11) was dependent on the gap distance from the open end of the probe body to the facepiece (*d*) and the relative permittivity ($\epsilon_r$) inside the active cavity, we expect that it would be simple to monitor pressure fluctuations using a modified OE-HCCR with a thin metal-film in place of the facepiece. Choosing a metal film with appropriate thickness would allow for the vibration of this membrane due to sound waves. Monitoring the magnitude of the S11 signal at the resonance frequency while sound waves vibrate the metal film would allow for the transfer of pressure waves into electrical signal, resulting in a new form of microphonics. Doing this would be the first step in the development of a sensor that could measure both pressure fluctuations and material changes simultaneously.

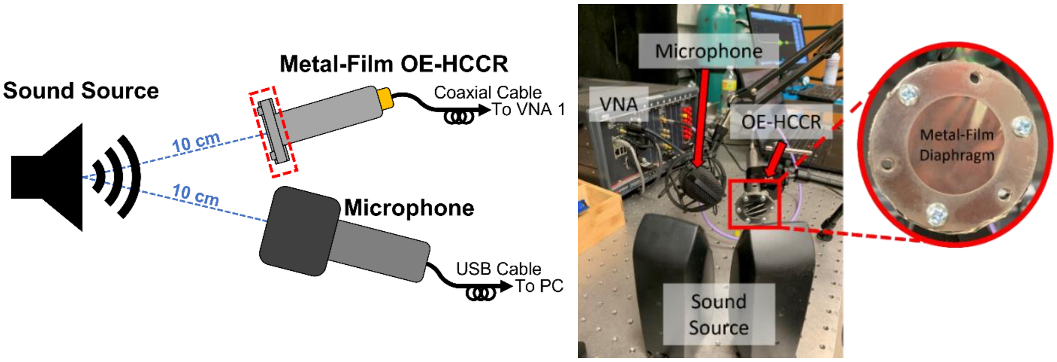

Figure 5.7: Experimental setup to validate an OE-HCCR-based microphone. Here, we aim to build a comparison of sound signals collected via a traditional microphone and a modified OE-HCCR with a thin metal-film diaphragm in place of the facepiece.

Figure 5.7 shows the experimental setup used to compare the sound signals collected via the traditional microphone and the modified OE-HCCR. In this set of experiments, the IF bandwidth was increased to 40 kHz. Keeping the same number of points due to equipment limitations, the length of signal that could be collected was significantly shortened, falling from over 45 seconds to roughly 2.5 seconds. Following the assumption that the maximum frequency in the audible range for humans is 20 kHz, the Nyquist sampling theorem required a sampling frequency of 40 kHz so as to not distort the signal. We used an online resource to generate two words each containing common phenomes (sounds) of the English language. Four with the resulting signals from both sensors shown in Figure 5.8 below.

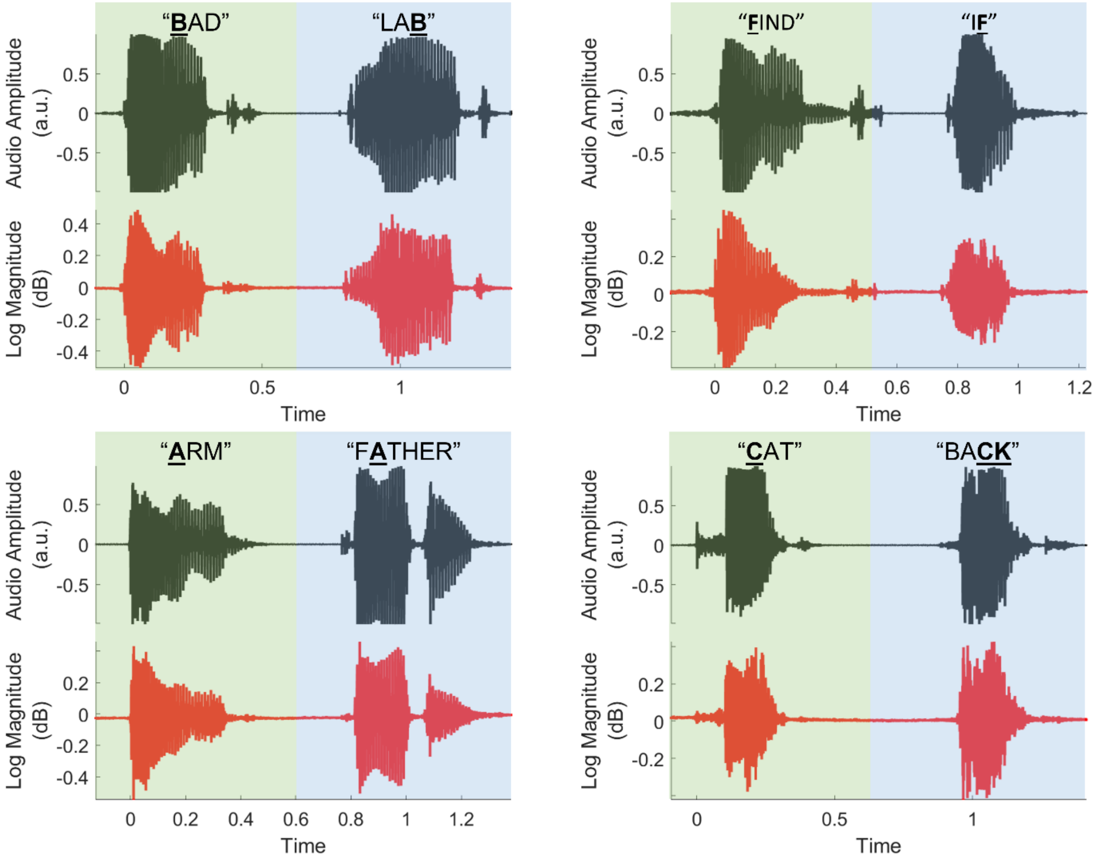

Figure 5.8: Comparison of sound signals from two sensors. Specifically, we compare a microphone signal (black) and modified OE-HCCR signal (red) for four combinations of phenomes.

**5.2.1. Combined Sound Wave and Matter Fluctuation Monitoring Using The Modified OE-HCCR.** Lastly, to continue our objective of creating a sensing technique that is sensitive to both sound and to changes in exhaled breath matter content, we performed a similar experiment to our previous two, this time boring a four small holes of approximately 1 $\mu$m diameter equally spaced around the outer edge of the metal-film diaphragm to serve as a breath inlet. Figure 5.9 shows the experimental setup for these trials.

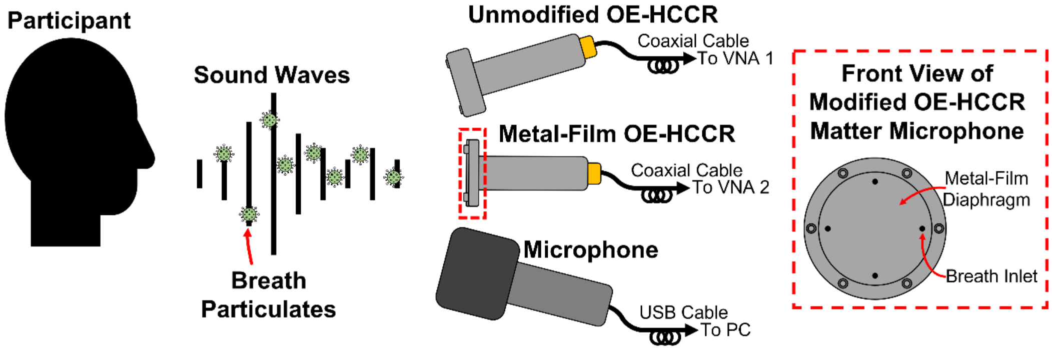

Figure 5.9: Experimental setup to validate the simultaneous collection of sound and permittivity signals. Here, a participant speaks towards three sensors. From top down: (1) the unmodified OE-HCCR will collect data pertaining to fluctuations in permittivity due to the exhaled matter in the breath; (2) the thin metal-film OE-HCCR ("Matter Microphone") will attempt to collect both sound and permittivity information; (3) a traditional microphone will collect sound data from pressure waves.

Here, we aimed to determine if it was possible to simultaneously collect the sound and permittivity signals using a single sensor. Thus, we arranged all three sensors facing a participant, who then repeated several selected phrases while the time transient signals from each sensor were recorded. The raw waveforms reported by each sensor for a single trial can be seen in Figure 5.10. The plots containing the data from other trials will be included in the supplemental data.

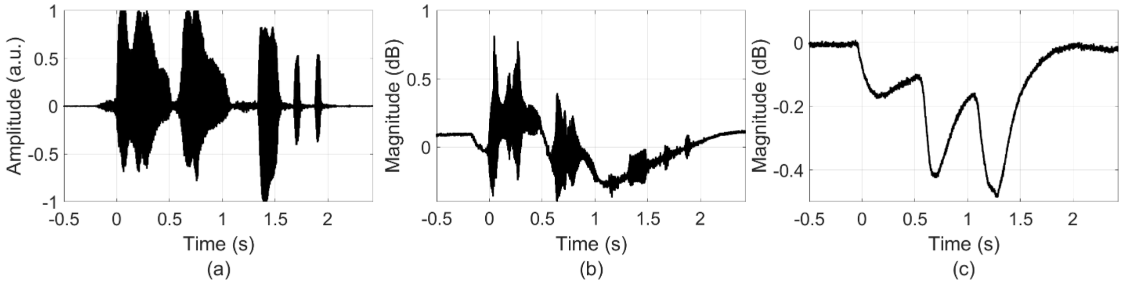

Figure 5.10: Unprocessed signals from three sensors. From left to right: (a) the raw audio signal captured by the microphone; (b) the combined matter-sound signal collected using the Matter Microphone; (c) the signal generated by permittivity fluctuations inside the active cavity of the unmodified OE-HCCR.

## 5.3. DISCUSSION

To process the data from section 5.2.4, a moving point average algorithm was used to parse the combined signal containing both audio and permittivity information into separate signals. First, the magnitude signal was interpolated to be the same number of points as the audio signal. Then, a moving point average with a fixed subset length of 100 points was used. Under the hypothesis that sound information would occur at higher frequency and permittivity information was more likely to be collected via the overall trend of the signal, we view the averaged signal as the permittivity signal and the sound signal as the original signal once the averaged signal was removed. The data was compared to the data collected by the respective dedicated sensor (e.g., the sensor dedicated to only detecting one of the parameters, either the microphone or the unmodified OE-HCCR depending on the parameter of interest). The two raw signals and processed signal corresponding to the sound data can be seen in Figure 5.11.

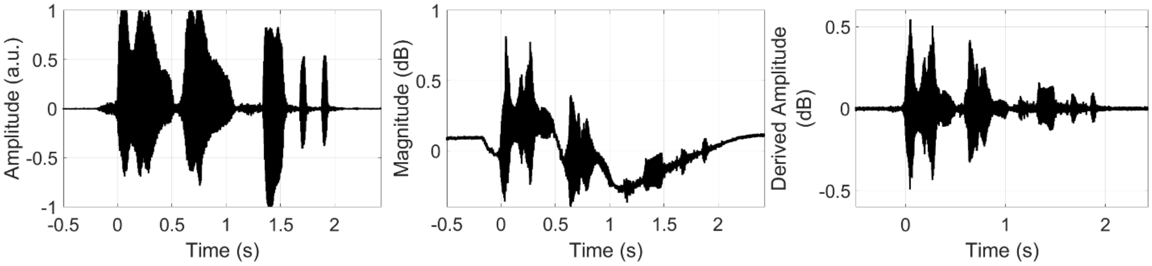

(a) (b) (c)

Figure 5.11: Processed sound signal from simultaneous collection of sound and permittivity fluctuations. Audio data collection using the thin metal-film OE-HCCR is compared to the microphone. (a) Raw microphone signal; (b) Combined audio and permittivity signal from the modified OE-HCCR; (c) the processed signal resulting from the subtraction of the moving point average, demonstrating the OE-HCCR's validity as a microphonics tool.

The raw microphone signal and the processed OE-HCCR signal show significant similarities. Noticeably, the amplitudes of the two signals peak at the same time instances and have similar form. There is more noticeable noise in the processed signal, supporting the need for a more rigid diaphragm. We suspect that optimizing the diaphragm thickness would allow for sound information to still be collected while dampening the background noise signal. No cross-correlation of the two signals was possible due to their conflicting file types. Meanwhile, the two raw signals and processed signal corresponding to the permittivity information can be seen in Figure 5.12.

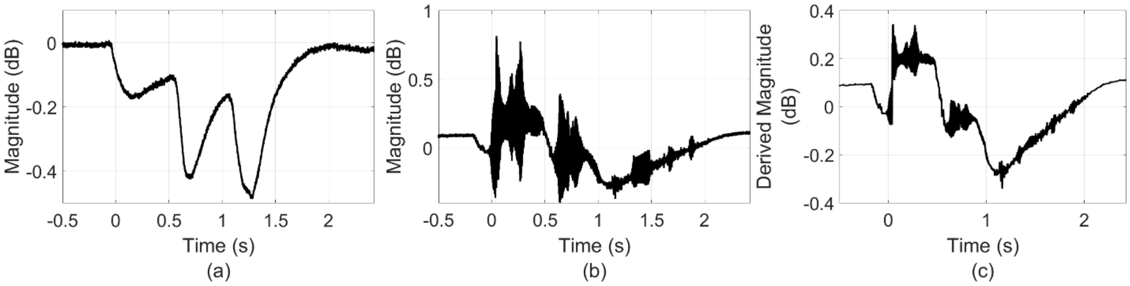

Figure 5.12: Processed permittivity signal from simultaneous collection of sound and permittivity fluctuations. Permittivity data collection using the thin metal-film OE-HCCR is compared to the unmodified OE-HCCR. (a) Raw unmodified OE-HCCR signal; (b) Combined audio and permittivity signal from the modified OE-HCCR; (c) the processed signal resulting from the moving point average.

Figure 5.12 showcases the processed permittivity signal from our combined sensor. Again, no cross-correlation of the signals was possible. However, there are still some common features in the two signals. Specifically, there are similarly spaced relative maximums and minimums across the two signals. Positive peaks of the processed signal last longer than those from the raw unmodified OE-HCCR signal, likely due to the variation of the gap distance, resulting in higher or lower relative permittivities in times of compression or expansion of the diaphragm, respectively. There is also noticeable noise in the processed signal, supporting the need for a wider moving-point average for the processing of this signal in specific.

## 5.4. RECOMMENDATIONS FOR FUTURE WORK

Here, we demonstrate the ability to collect information on two parameters simultaneously through the modification of our OE-HCCR sensing technology. Recommendations for future work include the optimization of the diaphragm’s thickness, a wider moving-point average for the processed permittivity signal, and the development of a micro-stripline implementation of our resonator. We suspect that a printed circuit board (PCB) implementation of our resonator would allow for the wide adoption of this technology for the collection of both audio and permittivity information, allowing for more robust machine learning algorithms that take both vocal and exhaled breath matter biomarkers into account.

# 6. CONCLUSIONS AND RECOMMENDATIONS FOR FUTURE WORK

## 6.1. CONCLUSIONS

The objective of this research is to advance the frontiers of permittivity-sensing technologies towards exhaled breath analysis. To this end, two variations of the open-ended hollow coaxial cable resonator are employed as the fundamental sensing platforms in this research.

In Paper I, we report a breath analyzer with ultra-high sensitivity and low limit of detection based on the OE-HCCR platform, offering phase-shift-amplified microwave resonance to detect compromised lung function through measures of exhalation flow and breath content.

The OE-HCCR's inexpensive, robust nature due to its all-metal structure and ease of signal demodulation suggest the potential to widely distribute the sensing platform to various applications of chemical sensing. The mathematical basis for the breath analyzer was reported, demonstrating the theoretical capability of the OE-HCCR as a breath analyzer with high dynamic range and low limit of detection. The combination of the platform's robust nature and high sensitivity make it an excellent candidate for use as a breath analyzer for continuous pre-screening of highly contagious pulmonary diseases in high traffic areas.

Experimental results support our hypothesis that volatile materials will initially dominate the breath transient signals. However, the volatile nature of these materials ensures their quick evacuation of the active cavity. Thus, any remaining signal offset is likely generated by the nonvolatile particulates that are often indicative of compromised lung function. Further, results verified the OE-HCCR breath analyzer's singular sensitivity to exhaled breath composition through experiments comparing the signals generated by tidal and rapidly exhaled breaths to those generated by ambient air. The final experiment set in Paper I compares the breath signatures of several individuals, demonstrating several distinct features of breath profiles that would later be supported through an IRB-approved breath transient study. Early analyses of breath transients led to suspicions that the falling edge of the time-transient signal offered the most insight, allowing for assumptions regarding the presence of nonvolatile content in breath.

Following the experiments detailed in Paper I, we sought approval to collect breath transient data from a larger population. After detailed deliberation on procedure and experimental setup, we were granted approval to collect breath transient data from 150 participants. While this process is ongoing, over 100 breath transient signals have been collected as of November 29th, 2022. Careful interpretation of these breath transients has revealed several distinct features common to all the time-transient signals acquired when the resonator is exposed to exhaled breath. So far, three regions of the breath transients have been identified and designated appropriately. Each of the regions, which are isolated from one another by phase peaks due to the resonators overcoupled phase condition, exhibit distinct features that offer further insight into the content of the exhaled breath. The first region, designated the active exhalation region, is the only region occurring concurrent to the participant exhaling into the resonator. This region is identified by the single rising edge and transitions to the aerosol digestion region following the first phase peak. Importantly, the first phase peak is the first feature to offer distinguishable patterns that can give insight into the content of the exhaled breath. Results show at least two patterns present following the first phase peak, denoted smooth and noisy. A smooth first peak is indicative of a consistent and stable phase curve as the curve shifts to lower frequencies with the influx of breath. Alternatively, a noisy first peak is indicative of modulation in the phase curve as it passes the CW frequency, suggesting slight variations in the resonators coupling condition. The next region, denoted the aerosol digestion region, marks the evacuation of volatile aerosols (i.e., water vapor, nitrogen, etc.) from the active cavity of the resonator. Here, we have identified three patterns that can give insight into breath matter content which have been designated as smooth phase reversal, phase curve modulation, and shelfed phase. Smooth phase reversal is indicative of a stable phase curve as the sweep direction reverses, meaning that the general shape of the phase curve is consistent when the curve is moving to lower frequencies and when it is moving to higher frequencies. Meanwhile, phase curve modulation suggests a change in the phase curve shape as the sweep direction reverses. Shelfed phase features indicate a late, yet rapid digestion of volatile materials due to the volatile particles that caused the volatile materials to remain up to the start of the shelf feature, respectively. The same phenomenon is likely to contribute to the hooked feature seen sometimes in the second phase peak of the breath transient signal. The last region, called the droplet evaporation region, can indicate the final presence of nonvolatile particles in breath. A gradual falling edge or a return to an offset phase level suggest nonvolatile materials that resisted removal from the active cavity. Increased significance of these two features indicate a higher volume of nonvolatile materials in the exhaled breath, either due to increased concentration or increased particle size distribution. The increased presence of these nonvolatile materials suggests unhealthy lung function.

Lastly, we report a modified OE-HCCR sensor developed for the simultaneous collection of both sound and permittivity information. Here, we aim to supplement the machine learning screening of pulmonary diseases through the analysis of vocal biomarkers by offering a second, independent dataset from the sound signal. First, we establish the independent nature of the two datasets, showing the singular collection of sound and permittivity information via a microphone and an OE-HCCR, respectively. Next, we demonstrate the simultaneous collection of both sound and permittivity information using a two-sensor system comprised of a microphone and a typical OE-HCCR. Lastly, we demonstrate a modified OE-HCCR that can simultaneously collect both datasets, which are later parsed through a moving-point average. Our hopes is that this research can serve as a supplement to machine learning algorithms, providing higher sensitivity and diagnostic accuracy, specifically as the number of diseases identified through machine learning techniques increases.

## 6.2. RECOMMENDATIONS FOR FUTURE WORK

Although the majority of the research presented in this thesis focuses on the survey of nonvolatile materials in exhaled breath, further work is being conducted to analyze the volatile content as well. Future research aims to validate the OE-HCCR breath analyzer as a diagnostic device to diseases such as SARS-CoV-2 and kidney disease by employing thin-film metal organic framework (MOF) structures inside the active cavity. By aligning several OE-HCCR sensors into an array, we hypothesize the survey of specific volatile organic compound (VOC) concentrations through the selective absorbance of the MOF thin-films. By monitoring the concentrations of several VOCs in exhaled breath, we suspect that the OE-HCCR array would exhibit sufficient sensitivity for the diagnosis of a variety of diseases. Further, employing hydrophobic MOF structures would remove the masking nature of water vapor from the breath transient signal, allowing for VOCs with lower permittivities to accurately be monitored. Exhaled breath volatiles offer even more insight into an individual's pulmonary function and disease state.

Next, the development of a micro-stripline open-ended cavity resonator could allow for more accurate and streamlined breath analysis. Although the stripline resonator sacrifices the robust all-metal structure of the OE-HCCR, the smaller form factor would allow for more rapid deployment as a diagnostic survey tool for various pulmonary diseases. A printed circuit board (PCB) implementation of our resonator structure could eliminate the need for a separate network analyzer anywhere that the resonator is being used. Removing this limitation could allow for the wide-spread adoption of microwave-resonance-based breath analysis

# REFERENCES

[1] C. Zhu, R. E. Gerald, Y. Chen, and J. Huang, “Probing the Theoretical Ultimate Limit of Coaxial Cable Sensing: Measuring Nanometer-Scale Displacements,” *IEEE Trans Microw Theory Tech*, vol. 68, no. 2, pp. 816–823, Feb. 2020, doi: 10.1109/TMTT.2019.2951099.

[2] C. Zhu, Y. Tang, J. Guo, R. E. Gerald, and J. Huang, “High-Temperature and High-Sensitivity Pressure Sensors Based on Microwave Resonators,” *IEEE Sens J*, vol. 21, no. 17, pp. 18781–18792, Sep. 2021, doi: 10.1109/JSEN.2021.3091589.

[3] C. Zhu, Y. Chen, R. E. Gerald, and J. Huang, “Ultrasensitive Open-Ended Coaxial Cable-Based Microwave Resonator Learns to Sense Impacts,” *IEEE Trans Instrum Meas*, vol. 70, 2021, doi: 10.1109/TIM.2020.3025655.

[4] S. Fan, K. Staebell, and D. Misra, “Static analysis of an open-ended coaxial line terminated by layered media,” *IEEE Trans Instrum Meas*, vol. 39, no. 2, pp. 435–437, Apr. 1990, doi: 10.1109/19.52531.

[5] J. Huang, T. Wei, T. Wang, J. Fan, and H. Xiao, “Control of critical coupling in a coiled coaxial cable resonator,” *Review of Scientific Instruments*, vol. 85, no. 5, 2014, doi: 10.1063/1.4873325.

[6] G. Laštovička-Medin and R. Pejanović, “Utilization of Low-Cost Sound Sensors with a built in Microphone as a Respiratory Pattern Sound Indicator and a Risk Mitigation Tool In response to COVID-19,” 2021.

[7] H. S. Maghded, K. Z. Ghafoor, A. S. Sadiq, K. Curran, D. B. Rawat, and K. Rabie, “A Novel AI-enabled Framework to Diagnose Coronavirus COVID-19 using Smartphone Embedded Sensors: Design Study,” in *Proceedings - 2020 IEEE 21st International Conference on Information Reuse and Integration for Data Science, IRI 2020*, Aug. 2020, pp. 180–187. doi: 10.1109/IRI49571.2020.00033.

[8] M. Alkhodari and A. H. Khandoker, “Detection of COVID-19 in smartphone-based breathing recordings: A pre-screening deep learning tool,” *PLoS One*, vol. 17, no. 1 January, Jan. 2022, doi: 10.1371/journal.pone.0262448.

[9] V. Despotovic, M. Ismael, M. Cornil, R. M. Call, and G. Fagherazzi, “Detection of COVID-19 from voice, cough and breathing patterns: Dataset and preliminary results,” *Comput Biol Med*, vol. 138, Nov. 2021, doi: 10.1016/j.compbiomed.2021.104944.

[10] S. Asadi, A. S. Wexler, C. D. Cappa, S. Barreda, N. M. Bouvier, and W. D. Ristenpart, “Aerosol emission and superemission during human speech increase with voice loudness,” *Sci Rep*, vol. 9, no. 1, Dec. 2019, doi: 10.1038/s41598-019-38808-z.

[11] S. Asadi, A. S. Wexler, C. D. Cappa, S. Barreda, N. M. Bouvier, and W. D. Ristenpartid, “Effect of voicing and articulation manner on aerosol particle emission during human speech,” 2020, doi: 10.1371/journal.pone.0227699.

[12] J. K. Gupta, C. H. Lin, and Q. Chen, “Characterizing exhaled airflow from breathing and talking,” *Indoor Air*, vol. 20, no. 1, pp. 31–39, Feb. 2010, doi: 10.1111/J.1600-0668.2009.00623.X.

# VITA

Peter Henry Holtmann graduated with a Bachelor of Science in Electrical Engineering from Missouri University of Science and Technology in May, 2021, where he balanced a rigorous course-load, campus employment, internships, and several leadership positions of various campus organizations that have allowed him to enhance his skills relevant to project management and academic research.

He joined the Lightwave Technology Lab at Missouri University of Science and Technology in the fall of 2020 as part of his accelerated master’s program. In May of 2023, Peter received his Masters of Science in Electrical Engineering from Missouri University of Science and Technology.

His research focused on the development of microwave-based sensing platforms for the detection of various airborne chemicals. Specifically, Peter performed experiments employing microwave-resonance for the analysis of exhaled breath.

Through the summers of his master’s program, Peter also worked as an electrical engineering intern at Sandia National Laboratories, where he worked in the Advanced RF group. He will return to Sandia full-time in January of 2022 as a senior microwave and sensor engineer.